Tracking Algorithms Under Boundary Layer Effects for Free-Space Optical Communications

by

Sue Zheng

S.B. Electrical Engineering and Computer Science
Massachusetts Institute of Technology, 2007

Submitted to the Department of Electrical Engineering and Computer Science
in partial fulfillment of the requirements for the degree of
Master of Engineering in Electrical Engineering and Computer Science
at the
MASSACHUSETTS INSTITUTE OF TECHNOLOGY
[September]
August 2007

Author ....
Department of Electrical Engineering and Computer Science
August 22, 2007

Certified by.........
Erich P. Ippen
Elihu Thompson Professor of Electrical Engineering
Professor of Physics
Thesis Supervisor

Certified by...
Jeffrey M. Roth
Technical Staff, MIT Lincoln Laboratory
Thesis Supervisor

Accepted by...
Arthur C. Smith
Chairman, Department Committee on Graduate Students

Tracking Algorithms Under Boundary Layer Effects for Free-Space Optical Communications

by

Sue Zheng

Submitted to the Department of Electrical Engineering and Computer Science
on August 22, 2007, in partial fulfillment of the
requirements for the degree of
Master of Engineering in Electrical Engineering and Computer Science

Abstract

Free-space optical communication requires accurate tracking to maintain links. The tracking problem between an aircraft and satellite becomes more difficult with the introduction of a turret on the aircraft for increased field-of-regard. In the case of a hemispherical turret, the disrupted airflow at the boundary layer can greatly distort the optical beam. A model of the communication link is created to compare the performance of several tracking algorithms. We investigate the best algorithm under various atmospheric conditions and signal-to-noise ratios.

Thesis Supervisor: Erich P. Ippen
Title: Elihu Thompson Professor of Electrical Engineering
Professor of Physics

Thesis Supervisor: Jeffrey M. Roth
Title: Technical Staff, MIT Lincoln Laboratory

Acknowledgments

This work was sponsored by the Department of the Air Force under Air Force Contract FA8721-05-C-0002. Opinions, interpretations, conclusions, and recommendations are those of the author and are not necessarily endorsed by the United States Government.

Contents

List of Figures

List of Tables

Chapter 1

Introduction

1.1 Free-Space Optical Communications

A multiple-access free-space optical network is currently under development. Several satellites will form the high bandwidth backbone of the network with a few of these satellites possessing multiple access capabilities - i.e., multiple users can communicate with the satellite at the same time. The network may include lower-earth orbit satellites and aircrafts.

A free-space optical (FSO) network offers many benefits, such as large network coverage and high data rates. Lasercom is also attractive because such systems are smaller, lighter and require less power than its radio-frequency (RF) counterpart. Because of the high frequency of operation in single mode FSO communications, the optical beam experiences low beam divergence, which allows for secure channels and reduced transmitter power. However, the narrow spread of the beam also requires very accurate tracking between two terminals to maintain the communications link.

This thesis examines the tracking problem between two terminals, specifically, a link between an aircraft and a satellite. Airborne lasercom is useful for extracting data into the satellite backbone network. The high capacity of lasercom yields high bandwidth not attainable with conventional RF communications. In airborne lasercom, factors such as atmospheric scintillation and boundary layer turbulence work to degrade the optical beam, negatively impacting the tracking system. In the following sections, we will describe how two terminals establish a communications link and the impact of the atmosphere.

1.1.1 Pointing, Acquisition and Tracking (PAT)

The Lasercom Interoperability Standard (LIS) describes the pointing, acquisition and tracking sequence for TSAT. The process for establishing a link between an aircraft and satellite involves several stages. In the first stage, the aircraft sends a broad beacon to the calculated satellite position. The beam width of the beacon is wide in comparison to the communications beam, however, it is still quite narrow (~250 μrad) and the aircraft must scan the sky with the beacon beam to lay power on the satellite.

When the satellite detects the beacon, the satellite returns a narrow beam back to the aircraft. Upon detecting the satellite downlink, the aircraft stops the scan and points a stable beacon beam to the satellite. Once the aircraft receives a stable return from the satellite, it sends the narrower communications beam to the satellite.

1.1.2 Beam Degradation

While transmitting from one terminal to the other, the optical beam experiences degradation due to the atmosphere. Scintillation results from the beam's traversal through layers of atmosphere; the effects worsen at lower altitudes where the atmosphere is denser. Turbulence at the aircraft-atmosphere interface results in boundary layer effects, which also worsen at lower altitudes.

Fluctuations in the index of refraction along the line-of-sight causes atmospheric scintillation. The optical beam received at a terminal experiences intensity fading due to scintillation if the aperture size is small compared to the coherence length r_0.

Scintillation can be addressed by automatic gain control or centroiding in the tracking control system and by coding and interleaving in the communications system. Both gain control and centroiding attempt to increase the power received. Coding and interleaving, on the other hand, attempt to correct errors that result from channel fading. Interleaving performs particularly well against burst errors, which are typical of channel fading.

Boundary layer effects are caused by the propagation of an optical beam through the layer of non-uniform air that surrounds an aircraft. The turbulent airflow at the boundary layer of the aircraft results in fluctuations in the air density which occur more quickly than those seen in scintillation.

When the beam is transmitted from the aircraft to the satellite, the boundary layer effects appear similar to scintillation but occur on a faster timescale since the satellite is located in the far-field of the disturbance. For the satellite, the problem of boundary layer effects may be dealt with in the same manner as scintillation; therefore, this thesis will focus on the impact of the boundary layer on tracking at the airborne terminal. Boundary layer effects at an airborne terminal result in phase disturbances rather than intensity fluctuations.

The introduction of a turret on an airborne terminal allows for a larger field-of-regard but also increases boundary layer effects. The turret protrudes from the exterior of the aircraft and encases the lasercom terminal. This placement permits the receiver to be mounted above the surface level of the aircraft, allowing a larger portion of the sky to be viewed, as illustrated in Fig. 1-1. However, it causes local disturbances in the airflow around the turret which contributes considerable phase distortion to the beam.

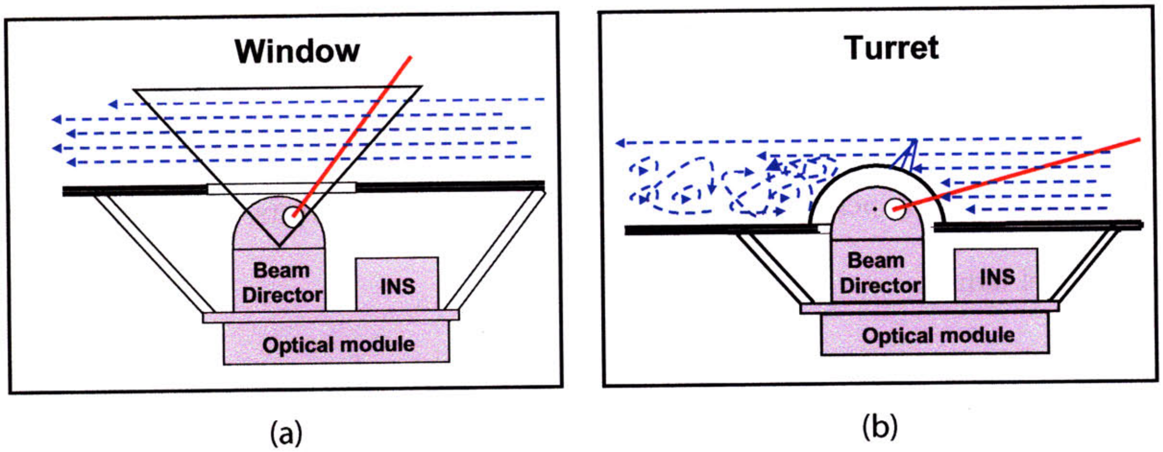

Figure 1-1: (a) Limited Field of Regard without a Turret. (b) Turret Increases Field of Regard and Boundary Layer Effects.

The nature of the flow disturbance is sensitive to the shape of the turret and view angle. Different turret shapes are currently being considered for implementation. Depending on the turret shape, there may be a quasi-static pressure buildup at the front of the turret resulting in optical distortions. In the downstream direction, there may be turbulent flow and the formation of eddies. Wavefront distortion in the downstream direction is expected to be more dynamic than in the forward direction. A quasi-static distortion is more easily dealt with than a dynamic one. Flow rates over the turret may even exceed the aircraft's velocity.

When the incoming optical beam is imaged onto the focal plane, the phase distortions can cause the beam's ideal Airy distribution to become multi-modal; this makes tracking more difficult because it introduces uncertainty in the exact location of the beam's center. Additionally, power from a multi-modal distribution couples poorly into the single-mode receiver, causing degraded performance in the communications system. This thesis will focus on the tracking aspect of the problem since loss of tracking would necessitate reacquisition of the beam.

1.2 Previous Work

There is interest in lasercom for reasons discussed previously and the US is progressing in the development of lasercom systems. MIT Lincoln Laboratory has a heritage in lasercom, having successfully demonstrated it. In this section, we will briefly discuss the lasercom programs at Lincoln Laboratory.

1.2.1 FSO Communications at MIT Lincoln Laboratory

The Geosynchronous Lightweight Technology Experiment (GeoLITE) satellite successfully demonstrated space-based lasercom in 2001. In this program, Lincoln Laboratory developed the lasercom payload on the GeoLITE satellite. The program demonstrated a high-rate communications link with a ground terminal.

In 2002, the GeoLITE satellite successfully communicated with an airborne terminal in the Airborne Laser Experiment (ALEX). In this demonstration, the aircraft had a conformal window, which resulted in minimal boundary layer effects and limited field of regard.

The Airborne Lasercom Terminal (ALT) program at Lincoln Laboratory was planned to mimic a satellite to aircraft link. A high-flying aircraft at an altitude greater than 60 kft was to be used as a pseudo satellite communicating with a low-flying aircraft. One of the goals of the program was to understand the air-to-space environment, such as the atmospheric channel and aircraft boundary layer. The program was designed to help the development and testing of channel and boundary layer models, which would in turn facilitate the development of optical terminals. MIT Lincoln Laboratory is carrying on this work in the Tracking Testbed program, which specifically focuses on PAT between an aircraft and a spacecraft using an experimental testbed to understand the impact of environmental conditions.

1.2.2 Boundary Layer Studies

Research is currently being conducted on the distortion of an optical beam caused by propagation through a boundary layer. Some of the research is focused on using computational fluid dynamics (CFD) to model the flow field around a hemispherical turret, both spatially and temporally, then analyzing the effect that such a flow field would have on an optical beam [4]. There have also been wind tunnel experiments to measure the optical distortion induced by the turbulent flow around a turret [3].

Actual flight measurements have not yet been obtained since such tests are expensive. As mentioned previously, ALT's goals include understanding the boundary layer effects and verifying the fidelity of CFD results. In our analysis, we will use CFD results to compare the performance of the different algorithms.

1.2.3 Tracking Algorithms

The different types of tracking algorithms we will consider in our analysis are described in this section. An algorithm may perform better than others only for particular view angles since the boundary layer effects vary.

A centroid tracker is often used to determine and track the center of a beam. The center of the beam is calculated to be at the centroid of the detected power intensity pattern on the FPA or quad cell detector. However, a centroid tracker is not ideal for every application. If the beam profile becomes distorted, it is possible for the centroid of the power intensity to fall far from the beam center. In the presence of strong disturbances, as may be the case with boundary layer effects, it is necessary to consider a more sophisticated algorithm.

A windowed centroid tracker is sometimes used to determine and track the center of a beam. The center of the beam is calculated to be at the centroid of the detected power intensity pattern within a window of radius R about the maximum intensity pixel on the FPA. The optimal window size will likely depend on the view angle of the airborne terminal, since the type of boundary layer effects seen are influenced by the view angle. A modification can be made to the windowed centroid, where the window center is chosen such that the window captures the most power at the FPA. These two variations can provide significantly different estimates if the FPA image contains multiple peaks. In the case of the former algorithm, the window is centered about the tallest peak; with the latter algorithm, the window could be centered about the broadest peak.

A threshold centroid is used to reduce the impact of noisy pixels. A threshold value, which is set above the noise level, is subtracted from all the pixels. Negative values are set to zero, then a centroid is computed. A peak tracker is also occasionally used for tracking. It simply chooses the maximum intensity pixel as the beam center. A peak tracker can perform very poorly when there is low signal-to-noise ratio (SNR).

1.3 Problem Statement

The tracking system ideally should continue to track in the presence of processes which degrade the optical beam. Our focus is on the tracking system at the airborne terminal in a FSO aircraft-to-satellite link. The performance of several different tracking algorithms to estimate and track the beam center will be compared. Since tracking is lost if the power received is too low for an extended period of time, the performance metric we consider is the average power delivered to the satellite.

Chapter 2

Problem Analysis

The incoming beam from the satellite enters through an aperture on the aircraft and is imaged onto the focal plane using a thin lens. The focal plane image is detected by a focal plane array. The tracking algorithm looks at the detected image and determines where to point the transmit beam, such that the power received by the satellite is maximized. In this chapter, we will analyze this problem and describe the simulation we use to compare algorithm performance.

2.1 Far-Field and Focal Plane Approximations

To begin our analysis, we use scalar diffraction theory to make approximations on the far-field and focal plane patterns. This yields a reciprocal relationship between the distribution of power at the satellite and the image detected on the focal plane array. This will simplify the problem of choosing where to point the transmit beam. In the following sections, we relate the far-field pattern at the satellite to the focal plane pattern at the aircraft.

2.1.1 Power Distribution in the Far-Field

Scalar diffraction theory has been shown to yield accurate predictions under certain conditions. The conditions are that:

1. The aperture size must be large relative to the wavelength; and
2. The diffracting field is observed not too close to the aperture.

These conditions are clearly satisfied in our situation, as the aperture to wavelength ratio we will consider is ~$10 \times 10^{-2} : 1.55 \times 10^{-6}$. A more thorough derivation of the scalar diffraction theory results which we use below can be found in [2].

From scalar diffraction theory, we have the Huygens-Fresnel principle which states that the field U at a location P_0 is related to the field at the aperture through

$$U(P_0) = \frac{1}{j\lambda} \iint\limits_{\Sigma} U(P_1) \frac{e^{jkr_{01}}}{r_{01}} \cos(\theta)\, ds, \tag{2.1}$$

where $U(P_0)$ and $U(P_1)$ are the fields at location P_0 and P_1 respectively. The integration happens over all points within the aperture Σ. $\vec{r}_{01}$ is the vector from P_0 to P_1 and θ is the angle between the normal $\hat{n}$ to the aperture and $\vec{r}_{01}$. We can interpret the observed field to be a superposition of secondary sources at every point P_1 in the aperture Σ. These secondary sources are diverging spherical waves $\frac{e^{jkr_{01}}}{r_{01}}$ with directivity $\cos(\theta)$ and a complex amplitude $U(P_1)$.

We are interested in finding the diffraction pattern on a plane parallel to the aperture plane, namely the far-field pattern at the satellite. Taking the z-axis to be normal to the two planes and using the Fresnel approximation, we find that the near-field distribution is

$$U(x,y) = \frac{e^{jkz}}{j\lambda z} \iint\limits_{-\infty}^{+\infty} U(\xi,\gamma) e^{j\frac{k}{2z}[(x-\xi)^2+(y-\gamma)^2]}\, d\xi\, d\gamma, \tag{2.2}$$

where (x, y) and (ξ, γ) are coordinates in the far-field and aperture planes respectively. Eqn. (2.2) can be rewritten as

$$U(x,y) = \frac{e^{jkz}}{j\lambda z} e^{j\frac{k}{2z}(x^2+y^2)} \iint\limits_{-\infty}^{+\infty} \left\{ U(\xi,\gamma) e^{j\frac{k}{2z}(\xi^2+\gamma^2)} \right\} e^{-j\frac{k}{z}(x\xi+y\gamma)}\, d\xi\, d\gamma. \tag{2.3}$$

Using the stronger Fraunhofer approximation,

$$z_0 \gg \frac{1}{2}k\left(\frac{D}{2}\right)^2 = \frac{2\pi}{\lambda}\frac{D^2}{8},$$

where z_0 is the normal distance between the two planes and D is the diameter of the aperture, we obtain the following for the far-field distribution:

$$U(x,y) = \frac{e^{jkz}}{j\lambda z} e^{j\frac{k}{2z}(x^2+y^2)} \iint\limits_{-\infty}^{+\infty} U(\xi,\gamma) e^{-j\frac{k}{z}(x\xi+y\gamma)}\, d\xi\, d\gamma. \tag{2.4}$$

Ignoring the multiplicative factors in front of the integral, the far-field distribution is a Fourier transform of the field at the aperture. The axes of the transform are scaled such that $f_x = \frac{x}{\lambda z}$ and $f_y = \frac{y}{\lambda z}$. We are within the Fraunhofer regime when finding the far-field pattern at the satellite, since the distance between the two terminals is approximately 3.5×10^7 m and the Fraunhofer approximation requires that $z_0 \gg$

$\frac{2\pi}{\lambda}\frac{D^2}{8} \approx 5 \times 10^3$ m, assuming an aperture diameter D of 10 cm.

To find the power distribution at the satellite, we are interested in the magnitude-squared of $U(x, y)$. The multiplicative factors in front of the integral in Eqn. (2.4) only scale the entire far-field power distribution, since the x- and y- dependencies disappear when taking the magnitude. Therefore, the power distribution at the satellite $P(x, y)$ becomes

$$P(x,y) \propto \left| \iint\limits_{-\infty}^{+\infty} U(\xi,\gamma) e^{-j\frac{k}{z}(x\xi+y\gamma)}\, d\xi\, d\gamma \right|^2 . \tag{2.5}$$

2.1.2 Image on Focal Plane Array

To find the pattern on the focal plane array, we need to consider the effect of a thin lens on an incident field $U_l(\xi, \gamma)$. Using the thin lens and paraxial approximations and neglecting a constant phase factor, we have

$$U_l'(\xi,\gamma) = U_l(\xi,\gamma) e^{-j\frac{k}{2f}(\xi^2+\gamma^2)}, \tag{2.6}$$

where $U_l'(\xi, \gamma)$ is the field immediately behind the lens and f is the focal length of the lens. Now, we use the Fresnel approximation to find the field at the focal plane, which lies in the near-field. From Eqn. (2.3) and Eqn. (2.6), we have the field at the focal plane $z = f$ is

$$U(x,y) = \frac{e^{jkf}}{j\lambda f} e^{j\frac{k}{2f}(x^2+y^2)} \iint\limits_{-\infty}^{+\infty} U_l(\xi,\gamma) e^{-j\frac{k}{f}(x\xi+y\gamma)}\, d\xi\, d\gamma \tag{2.7}$$

Ignoring the multiplicative terms in front of the integral, we see that the field at the focal plane is the Fourier transform of the field incident on the lens. The axes of the transform are scaled such that $f_x = \frac{x}{\lambda f}$ and $f_y = \frac{y}{\lambda f}$.

The focal plane array detects incoming light, which related to the intensity of the field. The field intensity is proportional to the magnitude-squared of the field. As before, the x- and y- dependencies of the multiplicative factor disappear and we have that the image on the focal plane array $I_{FP}(x, y)$ is

$$I_{FP}(x,y) \propto \left| e^{j\frac{k}{2f}(x^2+y^2)} \iint\limits_{-\infty}^{+\infty} U_l(\xi,\gamma) e^{-j\frac{k}{f}(x\xi+y\gamma)}\, d\xi\, d\gamma \right|^2 . \tag{2.8}$$

Thus, the pattern on the focal plane array is the same as the power distribution in the far-field up to a multiplicative factor. Note that the spatial scaling of the pattern is quite different. If we consider a setup where the aircraft has a detector at the focal plane to measure the focal plane distribution with an instrument field of view of $\frac{\lambda}{2D}$ per pixel and pixel size of 25 μm, the effective focal length f is 3.2 m. Assuming a satellite altitude of 35,000 km, the spatial scaling differs by a factor of 10^7. In the far-field, the satellite only sees a small portion of the pattern. The aircraft, on the other hand, essentially sees all of the transform distribution on the focal plane.

Since the far-field and the focal plane see the same pattern, we are able to approximate the power that is sent to the satellite by finding the power at a given point in the focal plane distribution and using an appropriate scaling factor. Using a fast steering mirror (FSM) to steer the outgoing beam and shift the far-field distribution, we can attempt to maximize power sent to the satellite. Having the outgoing beam and incoming beam share a common path which includes the FSM causes the pattern on the focal plane to shift as well. This results in a reciprocal relationship where maximizing power to the satellite becomes equivalent to maximizing the power on the focal plane at a given location. This is illustrated in Fig. 2-1, where the outgoing beam is co-linear with the center of the FPA. In this example, maximizing power to the satellite is equivalent to maximizing the intensity at the center of the FPA.

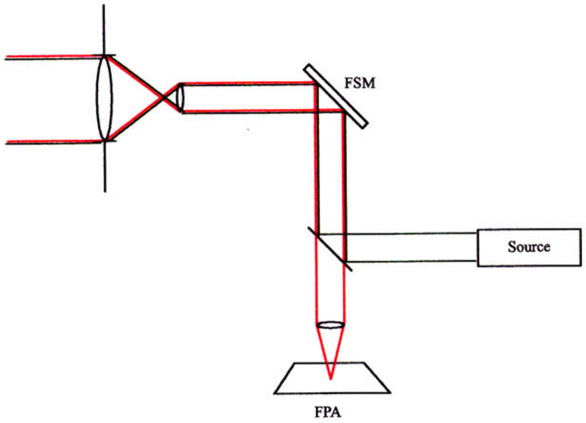

Figure 2-1: Outgoing Beam is Co-linear with Center of FPA

This reciprocal relationship simplifies the tracking problem. For the situation where there is no boundary layer, an Airy distribution is imaged onto the focal plane and the tracking system works to steer the peak of the distribution to the satellite's location on the focal plane. In the presence of boundary layer distortion, a multi-modal distribution may result. Peaks may rise and fall. Oscillatory switching between two or more peaks can produce a poor response in the tracking system since the mirror may have to steer through a null between the peaks. This causes a large drop in power at the satellite during the transition. It is undesirable for the satellite to experience an extended period of power dropout because the two terminals may lose tracking altogether and be required to repeat the acquisition procedure.

2.2 Algorithm Comparison

To compare the different tracking algorithms, we simulate the performance of the algorithms in the tracking system of an airborne terminal. Our figure of merit is the average power sent to satellite which can be determined from the focal plane array pattern. With an infinite bandwidth FSM and no readout noise, this problem would be greatly simplified. However, the bandwidth constraint requires that the tracking algorithm be selective in switching peaks with multi-modal distributions since the satellite may sit through a null for some appreciable amount of time. The read-out noise from focal plane array measurements can introduce pointing errors, resulting in power loss at the satellite. In the following sections, we will first describe the software simulation then discuss the variables which impact the tracking system and their chosen parameter values for the simulations.

2.2.1 Software Simulation

In the simulation, we assume that the satellite is always able to properly point at the aircraft. Therefore, the aircraft's pointing errors do not translate into pointing errors at the satellite. This assumption simplifies the simulations since we can focus on the aircraft side of the system; however, it also implies that the aircraft sends enough power to the satellite such that the satellite can accurately point back.

Given an FPA measurement, the algorithm makes an estimate of the pointing error and sends this to the tracking servo. The tracking servo filters the signal before sending it to the FSM. The FSM then steers the outgoing beam, translating the far-field power distribution, as well as the next incoming FPA measurement. The power to the satellite is estimated as proportional to the power at the center of the FPA image. This process then repeats, with the algorithm being applied to the next measurement. A block diagram of the software simulation is shown in Fig. 2-2. We will now discuss some of the relevant parameters and their values.

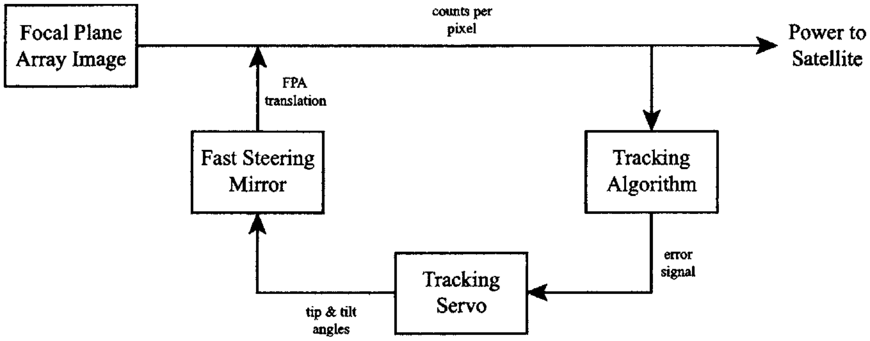

Figure 2-2: Block Diagram of Software Simulation

2.2.2 Aperture Size

Aperture size is a key factor that determines the average power received at the aircraft. The loss from optical devices and atmospheric fading is much less than the loss due to spreading of the beam while transmitting from the satellite to the aircraft. The aperture size determines the amount of light that enters the receiver; a larger aperture will capture more power.

The aperture size also determines how much of the boundary layer disturbance is viewed by the receiver. A system with a larger aperture will see more of the boundary layer disturbances. In addition to viewing more of the disturbances, a larger aperture requires a larger turret to encase the receiver, which impacts the type of boundary layer disturbance seen.

The aperture size is determined by link budget system engineering; the aperture is chosen to be large enough such that enough power is received for the communications system to perform close to the Shannon capacity, while being as small as possible to reduce size, weight, and power of the terminal. With the satellite in geosynchronous orbit transmitting a beam with 1 Watt average power, the power flux at the aircraft will be approximately 2.12×10^{-7} Watts/m^2, assuming a full beamwidth of 35 μrad from the satellite. Using the parameters consistent with previous programs, the aperture size is chosen to be 10 centimeters, resulting in 82 dB loss in received power. There is approximately 3 dB of loss in the receiver due to optics. Additionally, only 10% of the power is sent to the tracking system, with the rest going into the communications system. This results in a net loss of 95 dB for the tracking system.

2.2.3 Fast Steering Mirror

The fast steering mirror in the tracking system is used to steer the outgoing beam. The received beam also goes through the same FSM before being imaged onto the focal plane.

The two axes of the mirror, which are used to steer altitude and elevation, respond in a nearly decoupled manner so we will treat them as independent. Each axis has a transfer function which is modeled by a second order system with a natural frequency f_n of 120 Hz and a damping ratio ζ of 0.02, as shown in Fig. 2-3. The resulting second order transfer function is

$$H_{FSM}(s) = \frac{\omega_n^2}{s^2 + 2\zeta\omega_n s + \omega_n^2} \approx \frac{5.7 \times 10^5}{s^2 + 30s + 5.7 \times 10^5}. \tag{2.9}$$

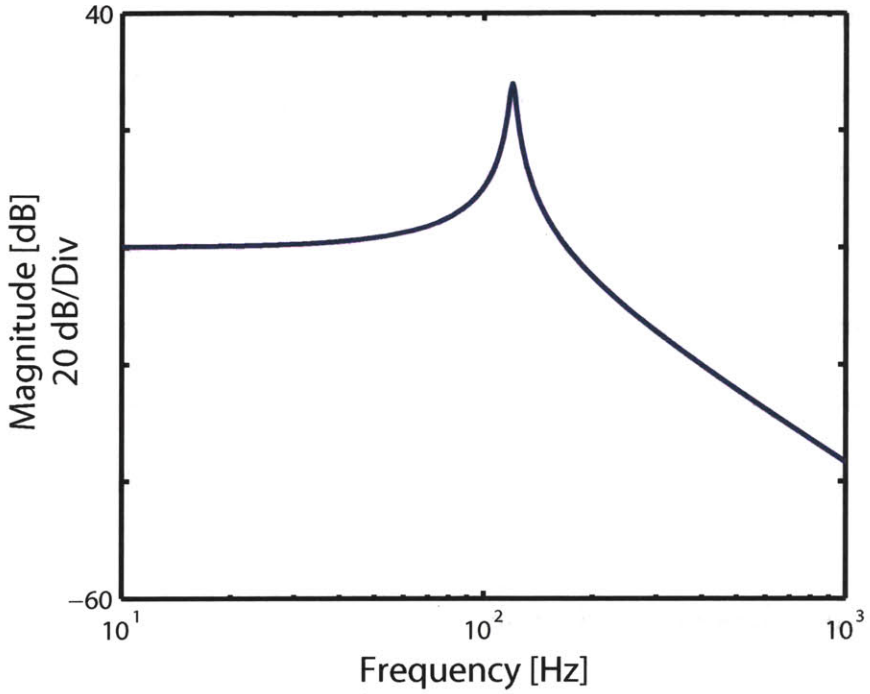

Figure 2-3: 2^{nd} order Approximation to FSM

2.2.4 Tracking Servo

We use a tracking servo and FSM similar to that used in previous FSO programs. The design of the servo was carried out by Professor Jim Roberge at MIT. To capture the effect of the tracking servo without requiring intricate details of the fully designed system, the tracking servo that is used in our simulations is a simplified model of Professor Roberge's design. The block diagram of this simplified model is shown in Fig. 2-4.

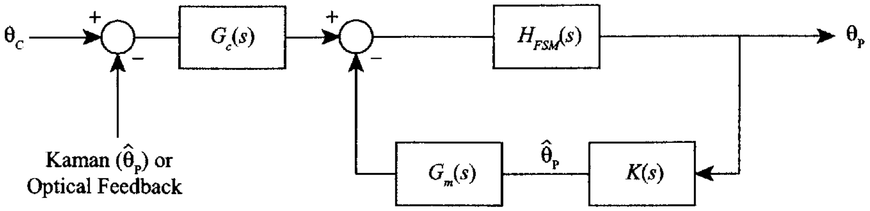

Figure 2-4: Block Diagram of Servo and FSM

From the previous section, we see that the FSM is very underdamped. Measurement from the FSM's Kaman sensor is used to wrap a minor feedback loop around the FSM. The response of the Kaman sensor $K(s)$ is a low pass with a cutoff that is much higher than our frequencies of interest. A derived rate network $G_m(s)$ is added to the feedback path to achieve a closed-loop response from the minor loop that is critically damped.

In the major loop, we prefer a first-order response from the loop transfer function during the acquisition stage of tracking since this provides good large-signal performance. We are primarily concerned about the tracking stage, where a second-order response provides better disturbance rejection. The major loop compensator adds two poles at the origin to achieve the second-order behavior at low frequencies and has a pair of zeros to cancel the low frequency pole-pair from the closed-loop transfer function of the minor loop. The compensator also includes a lead network to provide adequate phase margin at crossover. The resulting major loop compensator is

$$G_c(s) = \frac{(s + 2\pi \cdot 400)(s^2 + 6.54 \times 10^2 s + 6.31 \times 10^5)}{93.3s^2(\frac{1}{2\pi \cdot 5000}s + 1)}. \qquad (2.10)$$

The open loop response is plotted in Fig. 2-5. This system has a reasonable phase margin of 53.5 °, as shown in the figure.

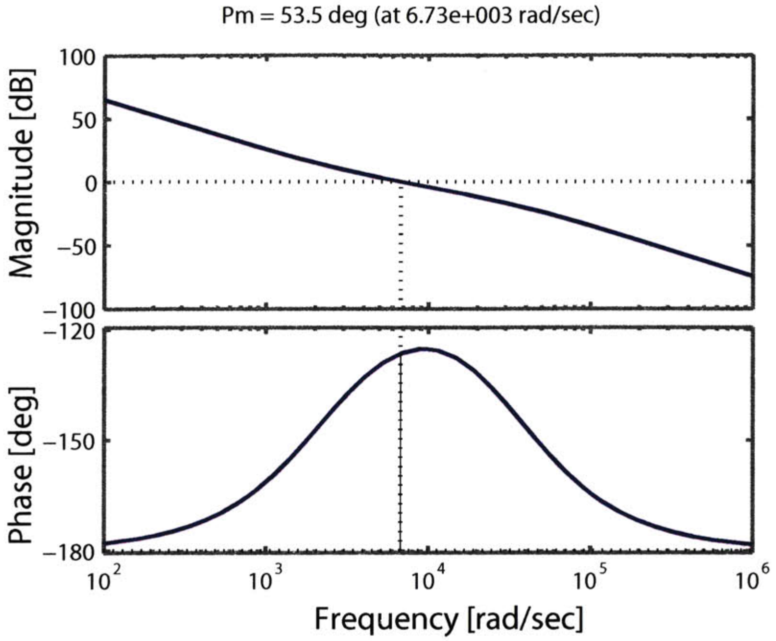

Figure 2-5: Open Loop Response

Assuming that we close the major loop using Kaman sensor measurements, the frequency response of the closed loop system is as shown in Fig. 2-6. The closed loop system has a bandwidth of approximately 1 kHz.

In our simulations, the major loop is closed using the tracking algorithm. The algorithm generates an error signal, based on the offset of the desired location from the center of the FPA.

2.2.5 Relative Power Received at Satellite

To estimate the power received at the satellite, we will use the reciprocal relationship developed earlier in this chapter. We have shown that the power sent to the satellite is approximately the power at the center of the focal plane, with appropriate scale factors.

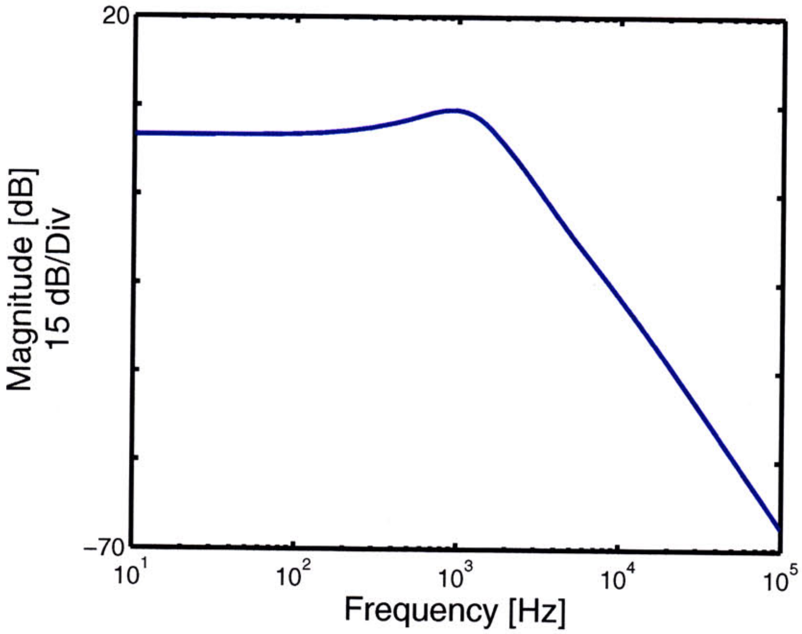

Figure 2-6: Closed Loop Response with Kaman Feedback

In our analysis, we will only consider the power sent to satellite relative to the ideal situation where the boundary layer distortions and atmospheric fading are absent and the aircraft achieves perfect pointing. This allows us to consider the degradation in power sent to the satellite that results from boundary layer effects and atmospheric fading as well as pointing errors from the tracking algorithm. In comparing algorithms, we use the time-averaged relative power to the satellite as our figure of merit.

2.3 Simulation of FPA Measurements

Ideally, the algorithms would be run on FPA measurements from a flight. However, flying an aircraft is a costly task and the measurements would depend on many factors such as turret shape and altitude. Using our knowledge of how different factors affect the measured data, we can simulate realistic FPA measurements for a variety of parameters. In this section, we describe how different parameters affect the measured data and how we simulate the measurements.

The primary parameters which affect the FPA measurements are the atmosphere, boundary layer, and measurement noise. In the absence of scintillation and boundary layer effects, the aperture has a uniform intensity and uniform phase field $U(x, y)$.

The atmosphere causes time-varying intensity fading $a(t)$ of the incoming beam while the boundary layer adds phase distortions $\Phi(x, y)$ to the beam. The received beam is then imaged down onto a focal plane array, which is equivalent to the magnitude-squared of the Fourier transform. The measuring device is the focal plane array of a camera which will introduce measurement error in the form of read-out noise $n(x, y, t)$. Additional details of each parameter are described in the following sections. The block diagram in Fig. 2-7 illustrates the simulation of FPA measurements.

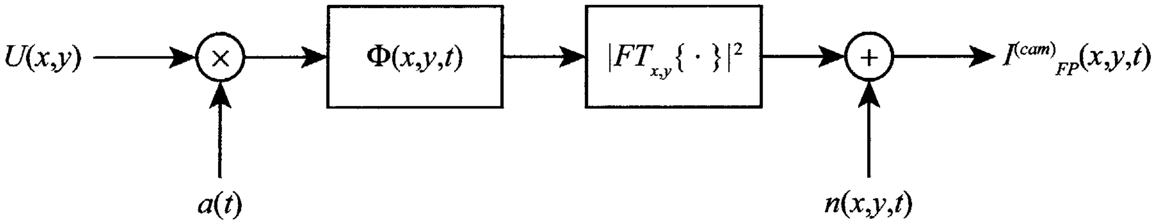

Figure 2-7: Block Diagram of FPA Measurement Simulation

2.3.1 Atmosphere

As mentioned previously, the atmosphere introduces intensity fading on the incoming optical beam. Widely used and shown to be a good representation of the atmosphere, the Kolmogorov model for the atmosphere attributes the phase disturbances in the wavefront to variations in the refractive index of the atmosphere [1,6,7]. This translates into fading when the beam propagates to the receiver. Since the aperture is small compared to the size of the pockets of air in the atmosphere, we approximate that there is uniform fading across the aperture and the atmosphere does not introduce any phase distortions.

The simulation of an atmospheric fading time series is described in excellent detail by Steven Michael [5]. We use his results in our simulations. To simulate a time series of atmospheric fading, an optical beam is propagated through vacuum to a phase screen. The phase screen contributes its phase to the beam and the beam is propagated to the next phase screen. This process is repeated until the beam reaches the receiver. The 10 phase screens in the path match the Kolmogorov model, with the impact of wind simulated by translation of phase screens across the beam.

Before we discuss the angle-dependent characteristics of atmospheric fading, we will define the reference frame. Azimuth (az) and elevation (el) angle definitions are illustrated in Fig. 2-8. The azimuth angle is the angle between the aircraft nose and the satellite, projected down onto the horizontal plane of the aircraft. Azimuth angle increases in the clockwise direction when viewed from above. The elevation angle is measured between the aircraft's horizontal plane and the satellite, increasing towards the zenith.

At an altitude of 29 kft, the typical fade has a 0-dB mean except when the beam is transmitted at very low elevation angles. At 11° elevation, the average fade is only 1 dB. There is greater fading at low elevations since the beam travels along the earth's surface, seeing more atmosphere and accumulating greater phase disturbances.

Unlike elevation angle, the azimuth angle doesn't impact the amount of phase dis-

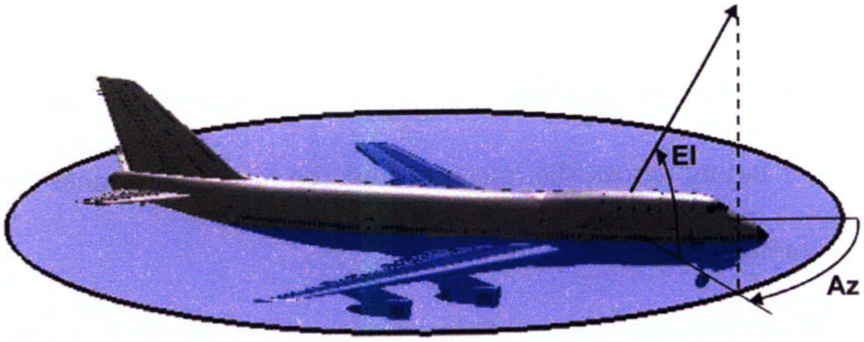

Figure 2-8: Azimuth and Elevation Angle

turbance accumulated; rather, it impacts the time-scale of the disturbances. At two closely spaced time instances, the beam travels through primarily the same pockets of air in the path of propagation if a beam is directed at 0° azimuth and 0° elevation. This results in slowly varying phase distortions. When a beam is directed at 90° azimuth and 0° elevation, the beam cuts through different pockets of air, resulting in more dynamic variations in atmospheric fading. By decomposing the beam direction into a component that is parallel to the aircraft's direction of motion and a component that is perpendicular, we appropriately scale the time axis of the simulated time-series for a given azimuth and elevation angle to simulate the time-series for all other azimuth angles.

Steven Michael [5] simulated different levels of turbulence by adjusting the turbulence model. The measure of turbulence strength, C_n^2, varies as a function of altitude, with the "Clear 1" model representing the average C_n^2 profile. We looked at two turbulence levels in our simulations, using 2× and 4× "Clear 1" models for moderately strong and very strong turbulence respectively. From the simulated time-series for various turbulence levels and elevation angles, we are able to obtain a time-series of atmospheric fading at all the relevant angles for our FPA simulation.

2.3.2 Boundary Layer

The boundary layer contributes phase variations which are sensitive to view angle, turret shape and turret location, among other things. Since these phase distortions have not been well characterized, we use simulated optical path difference (OPD) maps which have been derived from computational fluid dynamics (CFD) simulations.

The computational fluid dynamics simulations were carried out by Lockheed Martin. CFD uses numerical methods to solve for the airflow around the aircraft. The area around the turret is finely discretized to accurately capture flow phenomena. A coarser grid is used for locations which are further from the turret. A flow solver is then used to solve for the flow field about the aircraft.

This procedure is computationally intensive and, because of the many grid points and small time steps, can take several weeks to generate a short time series. Lockheed Martin has generated time series data of the air density about a turret on a U-2 aircraft. These air density values are then converted to indices of refraction, which affect the beam's speed of propagation and introduce path differences across the beam. An OPD map samples across the beam, generating a map of the path differences for the beam in units of wavelengths. Our simulation uses a time-series of OPD maps to simulate the effect of the boundary layer.

Specifically, the parameters of the CFD model we use are as follows. We consider a 16-inch super-hemispheric dome on a large superpod, located under the wing of a U-2 aircraft. A superpod is shown in Fig. 2-9. A super-hemispheric dome is chosen so that aircraft can utilize the full field of regard. The beam director/receiver is located at the spherical center of the hemisphere to be able to easily compensate for the wavefront distortion caused by the window. A regular hemispherical dome, on the other hand, would not be able to communicate at extremely low elevation angles. The duration of the simulation is 80 ms with 10 μs time steps. The CFD simulations model the aircraft flying at a speed of 0.7 Mach and an altitude of 29 kft. Results at a different altitude or airspeed can be approximated by scaling the OPD maps by $\rho \cdot M^2$, where M is the Mach number and ρ is the air density at the given altitude.

Figure 2-9: Superpod on a U-2 Aircraft

A diagram illustrating the flow density about a super-hemispherical turret on a superpod is shown in Fig. 2-10. The CFD simulations show a quasi-static pressure gradient in the forward direction. As the airflow accelerates over and around the turret, flow rates exceed the aircraft's velocity and may even become transonic. A shock wave forms high and forward on the turret, causing separation of flow and shedding of vortices behind the turret. Small motion of the shock wave induces significant phase changes as a result of the steep density gradient. The turbulent wake behind the turret causes dynamic density gradients.

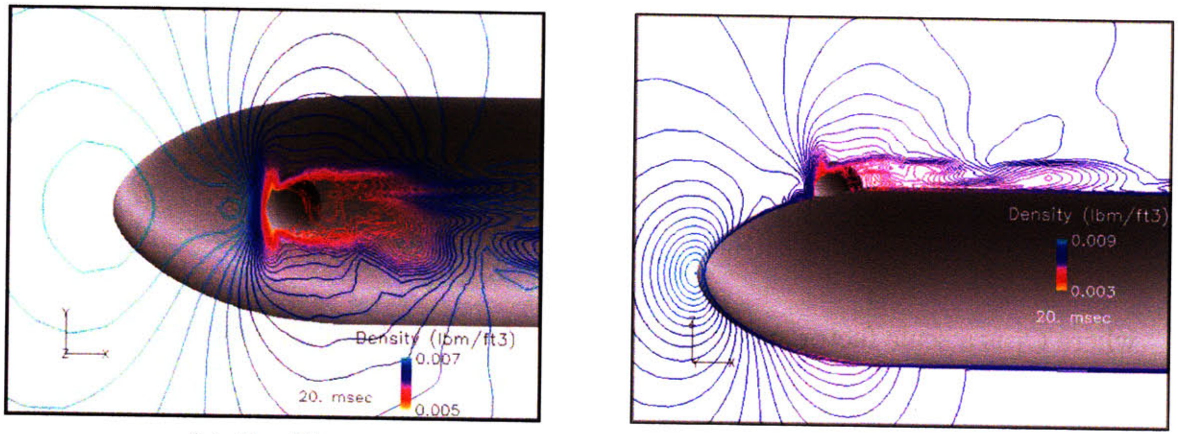

(a) Top View (b) Side View

Figure 2-10: Density Contours About Turret on a Superpod

2.3.3 Camera

The beam propagates through the atmosphere and boundary layer and is then imaged down onto the focal plane, where a camera detects the incoming light. A candidate camera for high-speed tracking in fast boundary layer effects is the Stratus camera from FLIR Systems (formerly Indigo). For this application, we would expect to run the camera at $22,000$ frames per sec and with an array size of 64×64 pixels. At this frame rate, the camera has rms noise of 140 electrons. Each pixel will have an instrument field of view of $\frac{1}{2}\frac{\lambda}{D}$, or approximately half a beam width[1]. This allows for a large portion of the sky to be viewed, while retaining resolution.

The incoming beam, as seen from the aircraft, would be approximately a plane wave, in the absence of scintillation and boundary layer effects. As described previously, scintillation and boundary layer effects introduce intensity fading and phase

---

[1] The beam width is approximated as $\frac{\lambda}{D}$. The actual beam width of a Gaussian beam is $\frac{4}{\pi}\frac{\lambda}{D} \approx 1.27 \times \frac{\lambda}{D}$.

distortions, respectively. Therefore, the incoming field at the aperture is

$$U_{FP}(x, y) = C_1 \sqrt{a(t)} e^{j2\pi\phi(\xi,\gamma,t)}, \tag{2.11}$$

where C_1 is a scale factor such that the time-averaged incoming power to the tracking system is -95 dB. $\phi(\xi, \gamma, t)$ is the optical path difference which varies across the aperture and with time. $a(t)$ is the time-varying intensity scaling from the atmosphere which is uniform across the aperture. Since the atmospheric scaling factor $a(t)$ scales the intensity of the beam, the field is scaled by $\sqrt{a(t)}$.

From Eqn. (2.8), we have that the pattern at the focal plane array is

$$I_{FP}(x, y, t) = C_3 a(t) \left| \iint\limits_{-\infty}^{+\infty} e^{j2\pi\phi(\xi,\gamma,t)} e^{-j\frac{k}{f}(x\xi+y\gamma)} \, d\xi \, d\gamma \right|^2, \tag{2.12}$$

where we have regrouped all constants into C_3 such that Eqn. (2.12) satisfies the average power constraint.

The camera has a finite pixel-size of $\delta \times \delta$, which results in sampling of the intensity profile at each pixel location. The sampled output from the camera $I_{FP}^{s}(k_x, k_y, t)$ is given below in Eqn. (2.13).

$$I_{FP}^{(s)}(k_x, k_y, t) = I_{FP}(x, y, t)\big|_{x=k_x\delta, y=k_y\delta}\,. \tag{2.13}$$

The effective focal length f of the lens is set such that the instrument field of view, Θ_i, of a pixel is $\frac{\lambda}{2D}$. Using the relationship

$$f \cdot \Theta_i = \delta,$$

we find that $f = \frac{2D\delta}{\lambda}$. Substituting this into Eqn. (2.13), we obtain

$$I^{(s)}_{FP}(k_x, k_y, t) = C_3 a(t) \left| \iint\limits_{-\infty}^{+\infty} \mathrm{e}^{j2\pi\phi(\xi,\gamma,t)} \mathrm{e}^{-j\frac{\pi}{D}(k_x\xi + k_y\gamma)}\, d\xi\, d\gamma \right|^2 \tag{2.14}$$

From our CFD results, we have OPD maps which contain the optical path difference at 64 × 64 points in rectangular coordinates, encompassing an inscribed 10-cm diameter circular aperture. Therefore, we have a spatially sampled version of $\phi(\xi, \gamma, t)$, which we denote as $\phi_s(n_\xi, n_\gamma, t)$, where n_ξ and n_γ are integers.

$$\phi_s(n_\xi, n_\gamma, t) = \phi(\xi, \gamma, t)\big|_{\xi = n_\xi \frac{D}{N}, \gamma = n_\gamma \frac{D}{N}}, \tag{2.15}$$

where N = 64. Using these results, we approximate the continuous time Fourier transform in Eqn. (2.14) with a discrete-time Fourier transform (DTFT). Additionally, we're interested in equally spaced samples of the transform, which correspond to the pixel values from the camera. This is equivalent to computing the discrete Fourier transform. Making the substitutions for ξ and γ in Eqn. (2.14) and approximating the integrals, we get

$$I^{(s)}_{FP}(k_x, k_y, t) \approx C_4 a(t) \left| \sum_{n_\gamma=0}^{N-1} \sum_{n_\xi=0}^{N-1} \mathrm{e}^{j2\pi\phi_s(n_\xi, n_\gamma, t)} \mathrm{e}^{-j\frac{2\pi}{2N}(k_x n_\xi + k_y n_\gamma)} \right|^2 . \tag{2.16}$$

From Eqn. (2.16), we easily see that the quantity within the absolute value is the $2N$-point DFT of the OPD map. Letting $\Phi(k_x, k_y, t)$ be the 2N-point DFT of $e^{j2\pi\phi_s(n_\xi,n_\gamma,t)}$, we can rewrite Eqn. (2.16) as

$$I^{(s)}_{FP}(k_x, k_y, t) \approx C_4 a(t) \left|\Phi(k_x, k_y, t)\right|^2 , \tag{2.17}$$

where C_4 is set such that the power constraint is satisfied.

The camera will integrate the photons for some time duration T_c before producing an output frame. In our simulations, we consider a camera rate of 20 kfps ($T_c = 50$ μs). The boundary layer effects are sampled at the higher frequency of 100 kfps ($T_{opd} = 10$ μs). We sum the response of the camera to five consecutive OPD maps to model the integration of photons and obtain a camera frame rate of 20 kfps.

$$I'_{FP}(k_x, k_y, n_t) = \int\limits_{n_t T_s}^{(n_t+1)T_s} I^{(s)}_{FP}(k_x, k_y, t)\, dt \tag{2.18}$$

$$\approx \sum_{k=0}^{4} C_4 a(n_t T_c + kT_{opd}) \left|\Phi(k_x, k_y, n_t T_c + kT_{opd})\right|^2 \tag{2.19}$$

Finally, the camera has electronics which introduce read-out noise $n(k_x, k_y, n_t)$. Read-out noise is well modeled as Gaussian distributed with mean m_n and variance σ_n^2. The read-out noise is pixel-wise and frame-wise independent. The output of the camera is thresholded at m_n to remove the mean noise; therefore, the effect of the read-out noise is modeled as a zero-mean Gaussian process. The Stratus camera has read-out noise with $\sigma_n = 140$. The resulting camera measurement is:

$$\begin{aligned} I_{FP}^{(Cam)}(k_x, k_y, n_t) &\approx n(k_x, k_y, n_t) \\ &+ \sum_{k=0}^{4} C_4 a(n_t T_c + kT_{opd}) \left|\Phi(k_x, k_y, n_t T_c + kT_{opd})\right|^2, \end{aligned} \tag{2.20}$$

where C_4 must satisfy the constraint that the power at the focal plane equals the time-averaged incoming power to the tracking system.

Chapter 3

Simulation Results

In this chapter, we will present some of our simulation results. First, we describe and examine performance in best and worst case scenarios. These scenarios provide bounds on the improvements made by the algorithms we consider. Next, we compare performance of the different algorithms under boundary layer effects. Then, we add atmospheric scintillation to the simulation and compare performance. Lastly, we look at the impact of variations in the signal-to-noise ratio at the FPA.

3.1 Best and Worst Case Bounds

In the Best Case, there is no read-out noise from the FPA and no bandwidth constraint from the tracking servo and FSM. It is best to use a peak algorithm in this situation since pointing at the peak yields the maximum power to the satellite. Performance under this situation is an upper bound on the average power delivered to the satellite. It captures the inherent degradation in performance that results from spreading of the outgoing beam by the boundary layer since pointing errors are absent in this noiseless, infinite-bandwidth situation.

The scenario for the Worst Case bound includes FPA read-out noise and bandwidth constraints from the FSM and tracking servo. In this case, we consider a centroid of the entire FPA as the worst algorithm; a centroid generally results in a poor estimate since no effort is made to reduce the noise in the estimate as in the case of the windowed and threshold centroid algorithms. Additionally, the asymmetric nature of the phase disturbance can skew the estimate far from the peak intensity or even onto a null between two or more peaks. The Worst Case provides a lower bound on performance, which the algorithms under comparison can improve upon.

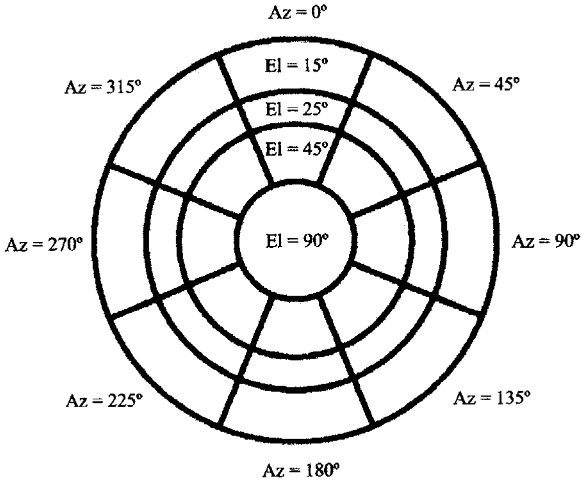

Figure 3-1: Sample Plot Illustrating Azimuth and Elevation Angles

Our results are presented in plots like the one shown in Fig. 3-1. The plot represents an overhead view of a hemispherical turret. Azimuth angle increases in the clockwise direction and elevation angle increases when approaching the center. The center represents 90° elevation. We ran simulations for look angles consisting of elevation angles at 15°, 25°, 45°, and 90°and azimuthal angles starting at 0° and increasing in increments of 45°.

In Fig. 3-1, azimuth and elevation labels are provided on the plot. The average degradation of performance in dB of the algorithm at a given look angle is represented on color scale at the appropriate azimuth and elevation angles of the turret. A single plot captures the performance of the algorithm across all look angles considered in the simulation. As described previously, performance calculations are relative to the case where boundary layer effects and atmospheric scintillation are absent and the aircraft achieves perfect pointing. Therefore, sources of performance degradation include boundary layer effects, atmospheric scintillation, and pointing errors.

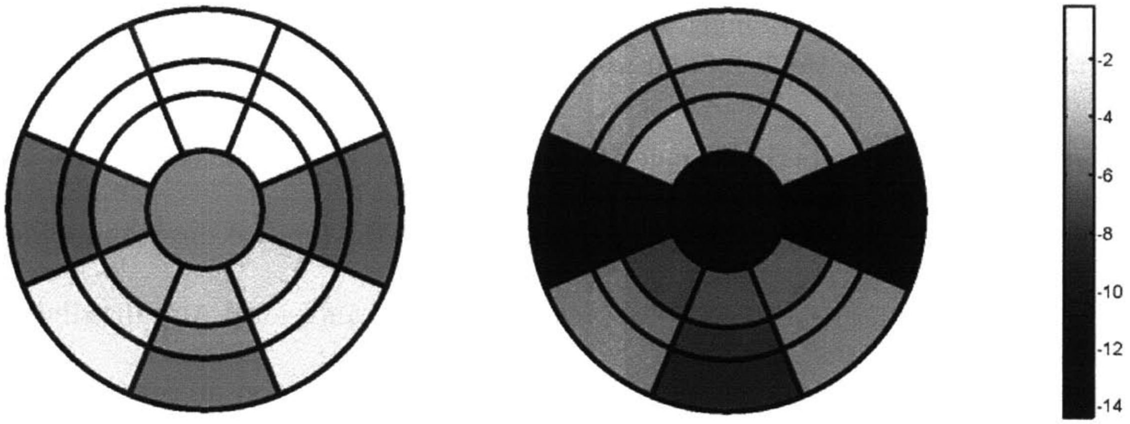

(a) Best Case

(b) Worst Case

Figure 3-2: Performance Bounds on Algorithms. Average Power to Satellite in dB Under: (a) Best Case (b) Worst Case

The results under the best and worst scenarios in the absence of atmospheric scintillation are presented in Fig. 3-2. As expected, we find that the average reduction in power to satellite is less in the best case than in the worst case for all look angles. A more quantitative comparison is available in Table 3.1. In the worst case scenario,

Look Angle		**Relative Loss in dB**		Look Angle		**Relative Loss in dB**	
El	Az	Best	Worst	El	Az	Best	Worst
15°	0°	0.16	4.43	45°	0°	0.15	4.88
15°	45°	0.20	4.93	45°	45°	0.20	4.74
15°	90°	6.42	13.78	45°	90°	5.29	14.42
15°	135°	1.43	5.47	45°	135°	2.22	6.72
15°	180°	5.83	10.73	45°	180°	3.00	7.62
15°	225°	1.62	5.66	45°	225°	3.25	8.00
15°	270°	6.27	13.83	45°	270°	5.03	13.03
15°	315°	0.19	4.65	45°	315°	0.19	4.29
25°	0°	0.15	4.88	90°	0°	4.95	13.36
25°	45°	0.21	4.34				
25°	90°	6.59	13.81				
25°	135°	1.46	5.49				
25°	180°	4.90	9.47				
25°	225°	1.79	5.93				
25°	270°	6.46	13.33				
25°	315°	0.20	4.90				

Table 3.1: Performance Bounds without Atmospheric Fading. The average power degradation in dB for the best- and worst-case at each look angle.

the centroid algorithm performs much worse even in the forward directions (-90°< az < 90°). There is little degradation in performance in the forward directions, where the distortion is quasi-static and the spreading of the beam's ideal Airy distribution by the boundary layer is minimal. There is greater degradation at ±90° azimuth, where the shock wave introduces strong phase distortions which can result in FPA images such as the one shown in Fig. 3-3.

At this azimuth angle, the FPA image is smeared and frequently becomes multi-modal, spreading its power across two or more peaks. This results in a reduction of power delivered to the satellite even before measurement noise has caused any pointing errors. From looking at the best case, we can see which look angles experience the most spreading in power due to the boundary layer.

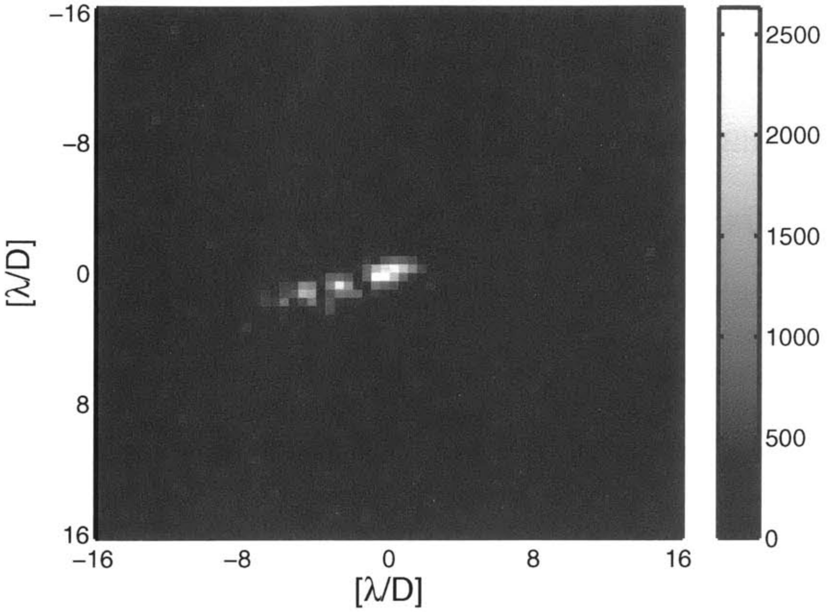

Figure 3-3: Example FPA Measurement at 90° Azimuth and 25° Elevation

At 180° azimuth, the turbulent flow behind the turret also results in strong spreading of the intensity profile. Lower elevation view angles image through more of the turbulent flow behind the turret, and experience greater power reduction. While the turret itself is symmetric, the plot of algorithm performance is slightly asymmetric. This is attributed in part to the short 80-ms duration of the time-series for the boundary layer, which is insufficient for averaging through all fluctuations. Asymmetric disturbances in the flow can cause asymmetry in performance. This is especially applicable in the downstream look angles, where the flow is more turbulent.

3.2 Boundary Layer

We now examine the performance of the algorithms under consideration in the presence of boundary layer effects, read-out noise, and bandwidth constraints from the

FSM and tracking servo. In each section, the plots will all be on the same color scale, which allows for direct comparison of different algorithms. Additionally, Table 3.2 contains the dB degradation in performance for all examined look angles under boundary layer distortions for each algorithm-parameter pair. The look angles vary along the rows and the columns contain the different algorithms.

First, we consider the Peak algorithm. The performance plot of this algorithm is shown in Fig. 3-4. Comparison of the Peak plot with the results from the Best Case in Fig. 3-2 reveal that Peak generally performs well across all look angles.

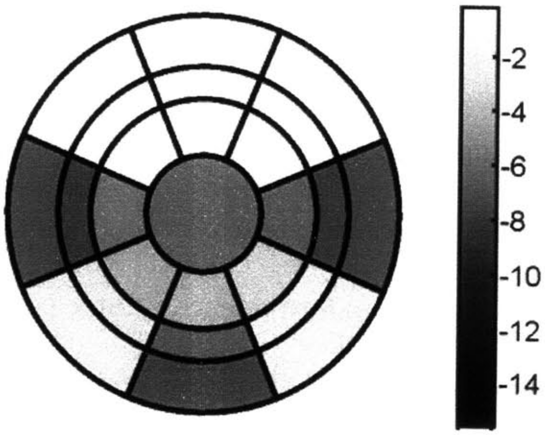

Figure 3-4: Relative Power to Satellite Using Peak Algorithm. Scale in dB.

The next algorithm is a windowed centroid, where the window is centered about the brightest intensity pixel on the FPA. This algorithm will be referred to as the Window Max since the window is centered about the maximum intensity pixel. We considered window sizes of radius of 1, 2, 4, and 8 pixels wide. The results of this algorithm at the various parameters are summarized in Fig. 3-5.

We also consider a windowed centroid where the window is centered about a pixel such that it captures the most intensity on the FPA. We will call this algorithm

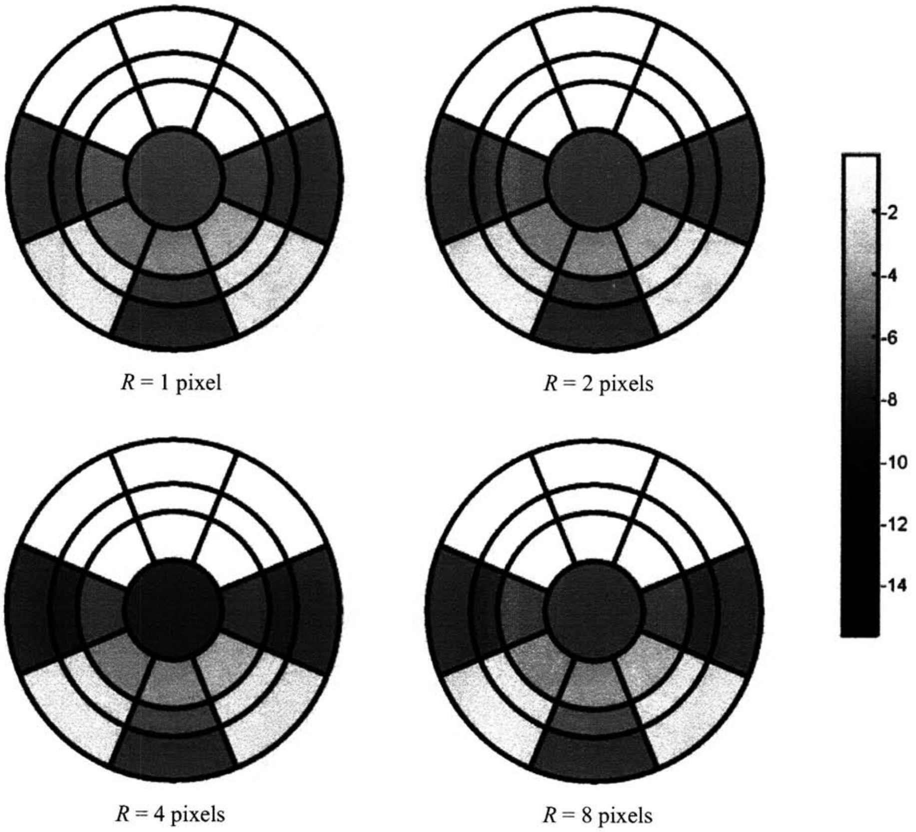

Figure 3-5: Relative Power to Satellite Using Window Max. Scale in dB.

Window Sum since the window is centered such that the sum of the pixel intensities within the window is maximized. Again, we looked at window sizes of radius 1, 2, 4, and 8 pixels. The results are shown in Fig. 3-6. At ±90° azimuth and $R = 8$ pixels, performance drops off sharply because the window becomes centered between two or more peaks to capture the most power; as a result, the aircraft sends the null between peaks to the satellite.

Finally, we looked at the performance of a threshold centroid algorithm, which will be called the Threshold algorithm. The threshold level, T was set at $1\times$, $2\times$, $4\times$, $8\times$, and $16\times$ the rms FPA noise. The performance plots are shown in Fig. 3-7. We find that the algorithm performs especially poorly for ±90° azimuth, since a centroid

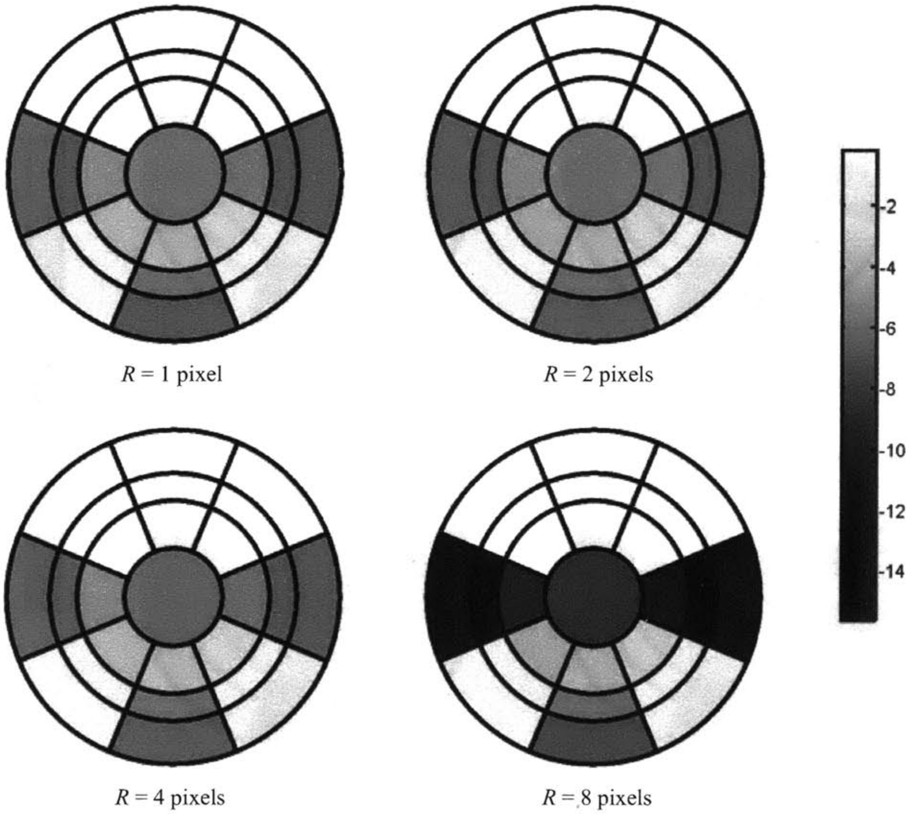

Figure 3-6: Relative Power to Satellite Using Window Sum. Scale in dB.

is taken of the entire FPA after it has been thresholded. The typical multi-modal distributions at those look angles result in a poor tracking estimate, as the estimate often does not point at a high intensity location. At extremely high threshold levels, such as $T = 16\times$, the signal may fall below the threshold level due to spreading of the beam intensity profile by the boundary layer. In these cases, the performance of the Threshold algorithm is undetermined since an estimate of the beam center cannot be made.

As seen in the plots, most algorithms perform quite similarly at the different look angles. Additionally, performance is usually not very sensitive to the parameter value of the algorithm. The difference in performance between some algorithm-parameter

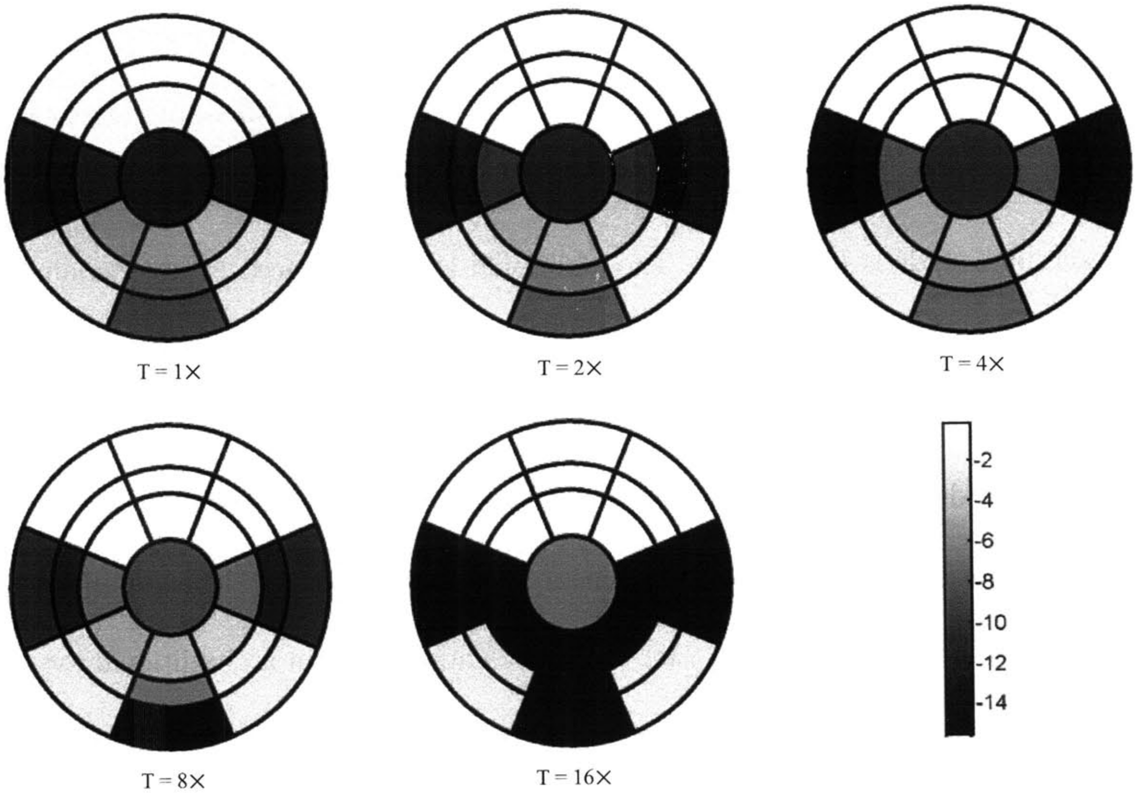

Figure 3-7: Relative Power to Satellite Using Threshold. Scale in dB.

pairs is so small that it is possible for the particular realization of simulated read-out noise to impact which algorithm performs better. Ten runs of the Peak algorithm at 270° azimuth and 25° elevation reveal a range in time-averaged performance from -7.33 to -7.45 dB, a difference of 0.12 dB. At this look angle, the boundary layer effects are prominent, causing greater sensitivity to variations in the noise. At 0° azimuth and 15° elevation, where the boundary effects are milder, the size of the performance range in 10 runs decreases to 6.6×10^{-4} dB. Pointing error sensitivity to read-out noise is typically very small compared to the total power degradation. The results presented are based on a single simulation run; keeping this in mind, we now look at a direct comparison of performance across algorithms and parameters.

A comparison of the algorithms is available in Table 3.2. Each row represents a different look angle and each column represents a different algorithm-parameter pair. In the table, the average performance degradation experienced by the best algorithm at each look angle is highlighted. The additional loss experienced by the remaining algorithms are also listed in the table. For example, at 90° azimuth and 15° elevation, the best algorithm is the Window Sum with a window radius of 2 pixels. The average performance degradation experienced by this algorithm-parameter pair is 6.89 dB. Peak, for the same look angle, experiences an additional 0.15 dB of average loss, bringing the net average loss to 7.04 dB. Some entries contain an additional loss of 0.00 dB, indicating that the difference in performance is under one-hundredth of a dB. This becomes important when recalling that variations in performance can occur due to the different read-out noise realizations. Entries in the table for the Threshold algorithm are unavailable when the signal drops below the threshold level and are marked with n/a.

Comparing the performance of the Peak algorithm in Table 3.2 with the Best Case in Table 3.1, we find that the additional reduction in power to the satellite due to pointing error from read-out noise and bandwidth constraints is small compared to the reduction in power caused by boundary layer induced beam spreading. While pointing error is negligible in the forward directions, it can decrease power to satellite by an additional 1.5 dB in directions with strong boundary layer distortions. At 180° azimuth and 15° elevation, the Peak algorithm in the Best Case has a performance degradation of 5.83 dB. After read-out noise and bandwidth constraints have been added, performance degradation increases to 7.35 dB.

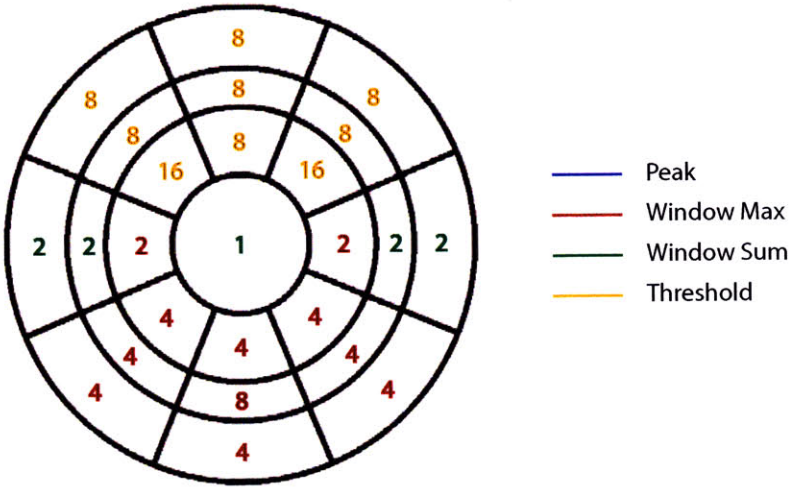

Figure 3-8: Best Algorithm at Each Look Angle without Atmospheric Scintillation

A plot of the best algorithm at the different look angles are shown in Fig. 3-8. The color at each look angle indicates the algorithm and the value indicates the parameter value. Since the Peak algorithm does not take any parameters, it is marked with a P. From this plot, we can note the following patterns. The Threshold algorithm with a high threshold level typically performs better than the others in the forward directions, where the beam distortions are static and the ideal Airy intensity profile is only mildly distorted. All algorithms perform very well at these look angles. In the backwards direction, the Window Max algorithm with a relatively large window size (~4–8 pixels in radius) best deals with the strong, rapidly-varying distortions. Lastly, at the look angles to the side and top of the turret, the windowed centroid algorithms with a small window size is best for dealing with the multi-modal distributions on the FPA that result from the shock wave.

In the next section, we will examine the performance of the algorithms when the impact of atmospheric fading is introduced into the model.

Look Angle		**Relative Loss in dB**														
		Peak	Window Max				Window Sum				Threshold					
El	Az	N/A	1	2	4	8	1	2	4	8	1	2	4	8	16
15°	0°	0.00	0.05	0.01	0.00	0.01	0.05	0.01	0.01	0.06	0.45	0.06	0.00	**0.16**	0.00
15°	45°	0.00	0.05	0.01	0.00	0.01	0.05	0.01	0.01	0.05	0.38	0.06	0.00	**0.20**	0.00
15°	90°	0.15	0.28	0.27	0.37	0.75	0.10	**6.89**	0.86	6.12	5.78	6.16	7.27	4.38	n/a
15°	135°	0.05	0.01	0.00	**1.51**	0.03	0.02	0.03	0.02	0.11	0.59	0.11	0.05	0.06	0.07
15°	180°	0.13	0.23	0.17	**7.22**	0.07	0.20	0.22	0.02	1.04	1.61	0.52	0.03	n/a	n/a
15°	225°	0.06	0.04	0.03	**1.73**	0.03	0.06	0.07	0.03	0.09	0.67	0.12	0.06	0.08	0.09
15°	270°	0.30	0.32	0.28	0.32	0.85	0.09	**6.77**	1.13	6.61	5.83	6.25	7.57	4.21	n/a
15°	315°	0.00	0.05	0.01	0.00	0.01	0.05	0.01	0.01	0.07	0.36	0.06	0.00	**0.19**	0.00
25°	0°	0.00	0.05	0.01	0.00	0.01	0.05	0.01	0.01	0.05	0.36	0.05	0.00	**0.15**	0.00
25°	45°	0.00	0.05	0.01	0.00	0.01	0.05	0.01	0.01	0.06	0.39	0.05	0.00	**0.21**	0.00
25°	90°	0.46	0.53	0.47	0.48	1.08	0.03	**6.78**	1.50	8.26	7.06	8.17	8.84	5.29	n/a
25°	135°	0.08	0.00	0.03	**1.61**	0.01	0.01	0.06	0.02	0.06	0.84	0.12	0.07	0.10	0.11
25°	180°	0.27	0.33	0.32	0.10	**6.08**	0.33	0.42	0.00	0.50	1.37	0.31	0.03	0.10	n/a
25°	225°	0.06	0.04	0.04	**1.95**	0.04	0.04	0.06	0.03	0.11	0.63	0.14	0.04	0.06	0.08
25°	270°	0.70	0.67	0.70	0.62	1.43	0.11	**6.77**	1.88	6.81	6.22	6.64	7.26	5.23	n/a
25°	315°	0.00	0.05	0.01	0.00	0.01	0.05	0.01	0.01	0.05	0.48	0.49	0.00	**0.20**	0.00
45°	0°	0.00	0.05	0.01	0.00	0.01	0.05	0.01	0.01	0.06	0.37	0.05	0.00	**0.15**	0.00
45°	45°	0.00	0.05	0.01	0.00	0.01	0.05	0.01	0.01	0.05	0.37	0.05	0.00	0.00	**0.20**
45°	90°	0.03	0.04	**5.70**	0.62	0.89	0.04	0.85	1.59	6.94	6.39	4.68	2.42	1.08	n/a
45°	135°	0.12	0.09	0.09	**2.83**	0.05	0.09	0.16	0.05	0.19	0.94	0.17	0.05	0.08	n/a [1]
45°	180°	0.13	0.09	0.11	**3.66**	0.16	0.10	0.23	0.09	0.38	1.14	0.31	0.13	0.13	n/a
45°	225°	0.07	0.04	0.12	**4.14**	0.08	0.12	0.30	0.07	0.35	1.07	0.28	0.07	0.11	n/a
45°	270°	0.00	0.01	**5.32**	0.35	1.25	0.03	0.55	1.40	6.44	6.03	4.70	2.59	1.54	9.86
45°	315°	0.00	0.05	0.01	0.00	0.02	0.05	0.01	0.01	0.07	0.38	0.06	0.00	0.00	**0.19**
90°	0°	0.01	0.06	0.02	0.66	1.25	**5.79**	0.53	2.60	4.27	6.40	5.82	4.74	2.44	1.11

Table 3.2: Performance Comparison of All Algorithms Without Atmospheric Fading. The average power degradation in dB for the best-performing algorithm at each look angle is highlighted. The remaining entries contain the additional degradation experienced by the other algorithms.

3.3 Boundary Layer and Scintillation

In this section, we are interested in the ability of algorithms to track through both atmospheric fading and boundary layer effects. We examine performance at two levels of atmospheric turbulence: 2× and 4× “Clear 1”. However, the short duration of the boundary layer time-series may limit our ability to capture the algorithms' performance during various fades since atmospheric fading occurs on a much slower time-scale than boundary layer effects.

3.3.1 Moderate Atmospheric Turbulence

First, we examine performance with moderate atmospheric turbulence. Plots of algorithm performance are shown in Fig. 3-10. These results are quite similar to the case without atmospheric scintillation. A more precise comparison of the algorithms' performance is available in the appendix on Table A.1.

Occasionally, the particular time-series realization of atmospheric fading used in our simulations has a time-average slightly greater than 0 dB, which accounts for average power in particular look angles being greater than in the previous situation without fading. This can cause the average dB degradation shown in Table A.1 to be negative, reflecting the gain from the atmosphere. This only occurs in the forward directions, where boundary layer effects are minimal.

The best algorithm-parameter pair plot is shown in Fig. 3-9. We start to see asymmetry arising in this plot, but the difference in dB performance of the asymmetric algorithms is very small. Peak is optimal at 90° azimuth and 45° elevation, while

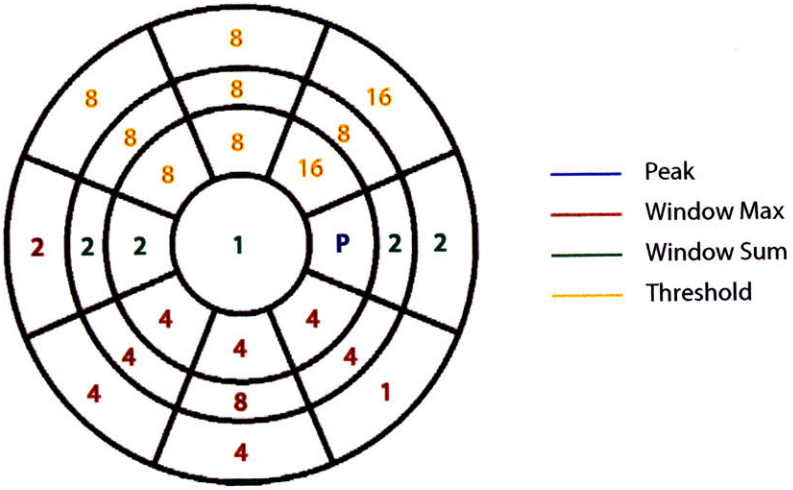

Figure 3-9: Best Algorithm at Each Look Angle at 2× “Clear 1”

Window Max with a radius of 2 is optimal at -90° azimuth. Window Max experiences only an additional 0.01 dB loss over Peak at 90° azimuth and Peak experiences an additional 0.06 dB at -90° azimuth. Again, this is most probably caused by differences in the noise realization or asymmetric airflow about the turret.

There is very little additional loss from atmospheric fading. We generally find the same pattern for best algorithms as before - high threshold in the forward directions and so forth. It appears that the boundary layer is the more prominent factor in determining the tracking algorithm for moderate atmospheric turbulence. In the next section, we examine the effect of stronger fading.

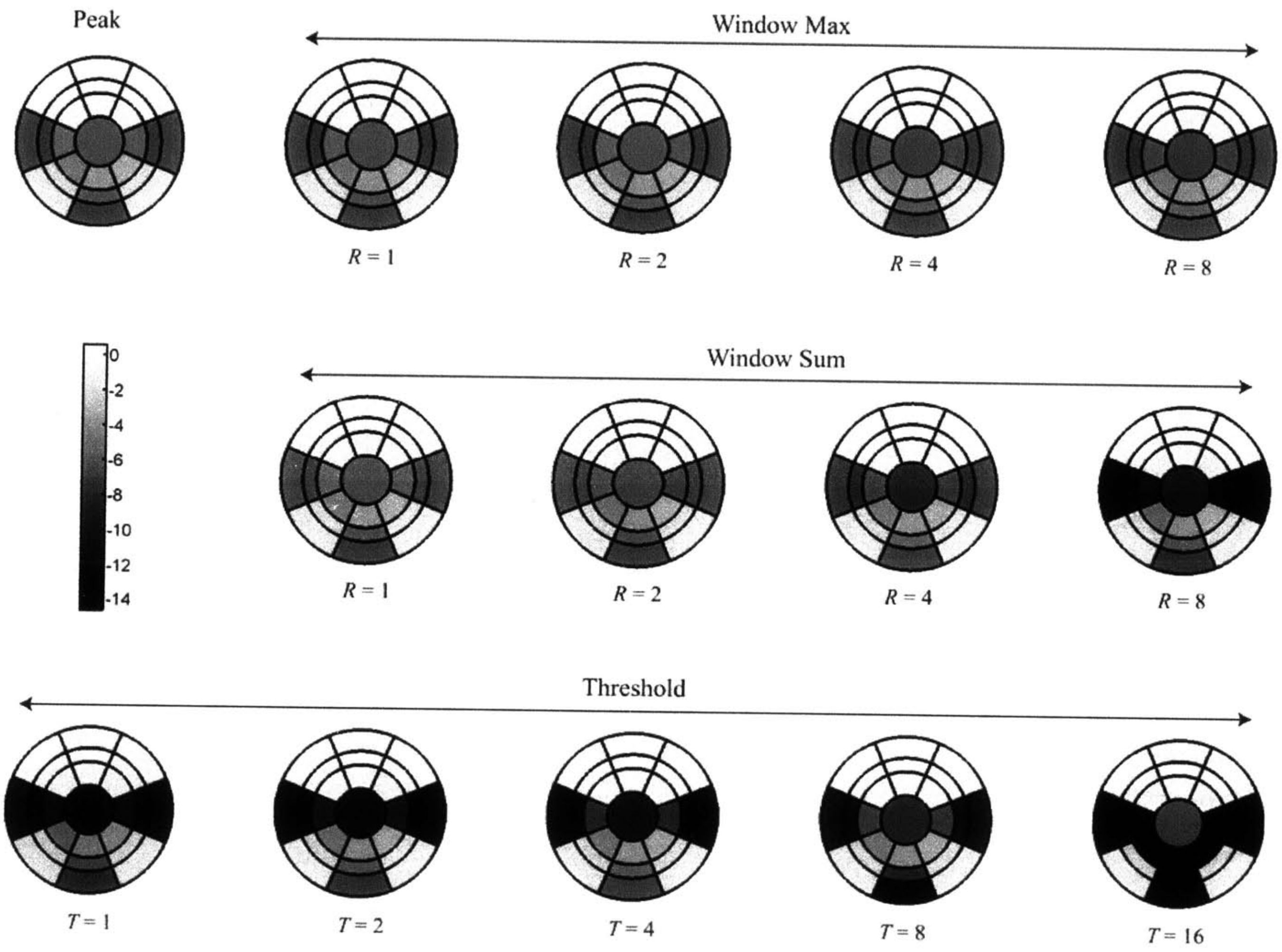

Figure 3-10: Algorithm Performance at 2× "Clear 1". Scale in dB.

3.3.2 Strong Atmospheric Turbulence

Seeing that there is little additional loss from moderate atmospheric turbulence, we are interested in the performance degradation that results from strong atmospheric turbulence. Fig. 3-11 shows the best algorithm at each look angle and Fig. 3-12 contains the performance plot for all the algorithms. Results are not available at 90° elevation, but atmospheric fading is milder for that look angle.

We would expect degraded performance at low elevation angles, where the impact of atmospheric fading is largest. Table A.2 contains the tabulated results. Comparison of Table A.1 with Table A.2 reveals that again there is little change in the dB performance degradation. In the next section, we will examine algorithm performance at a various SNR levels.

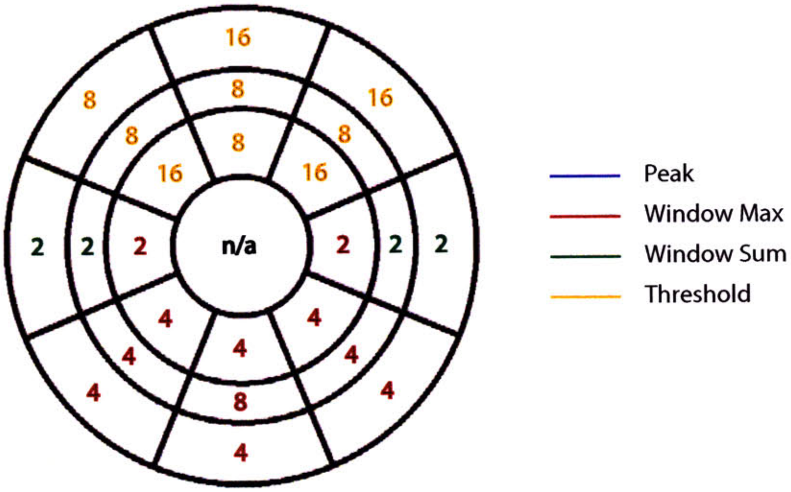

Figure 3-11: Best Algorithm at Each Look Angle at 4× "Clear 1"

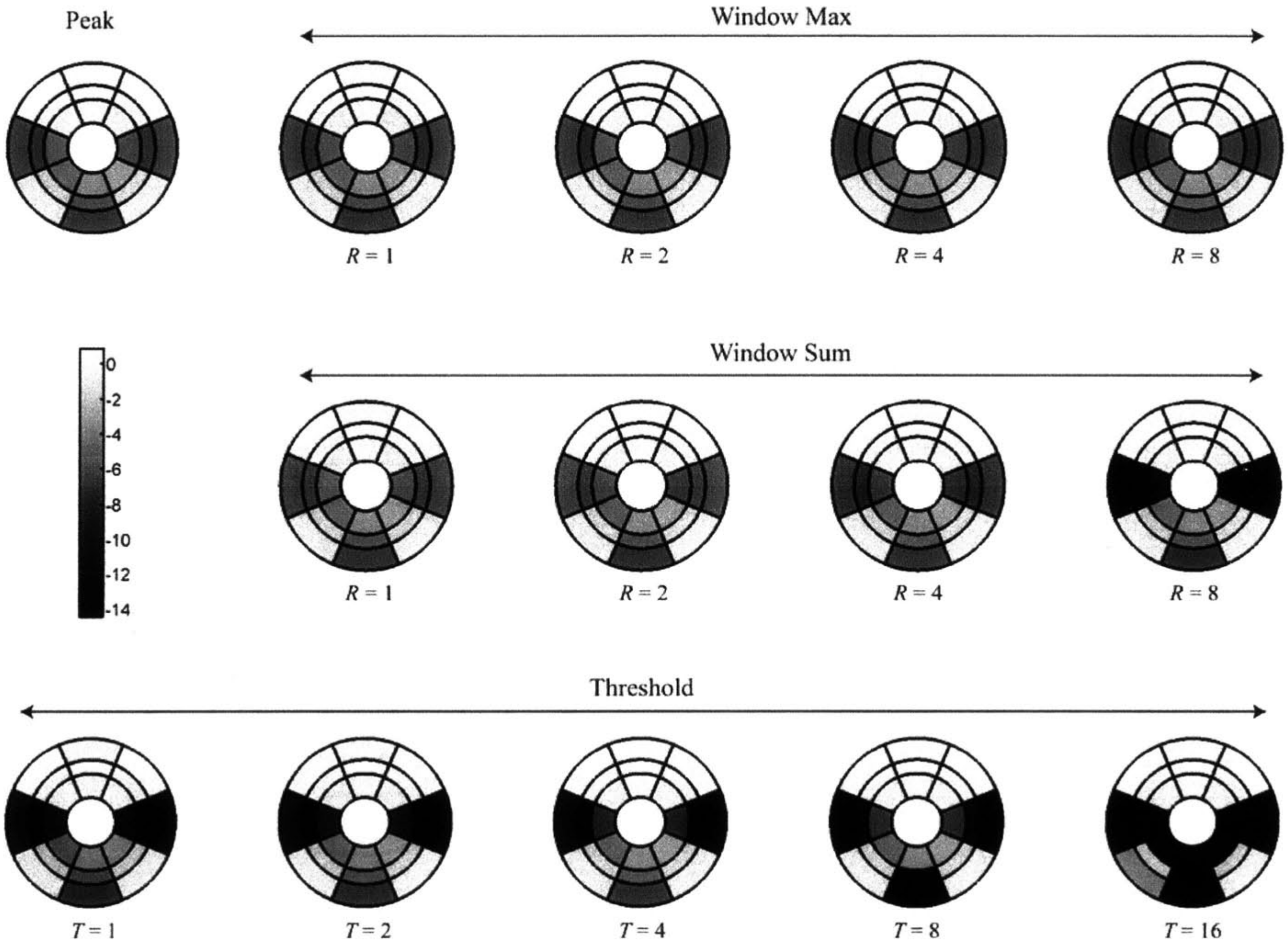

Figure 3-12: Algorithm Performance at 4× "Clear 1". Scale in dB.

3.4 Signal-to-Noise Ratio

In this last section, we consider how much gain or loss in performance is achieved by varying the SNR. First we look at how much performance improves when SNR is increased by a factor of 2, which occurs if the fraction of received power being sent to the tracking system were doubled. Then we look at how much performance degrades when we halve the SNR. In both situations, 2× "Clear 1" is used for the atmospheric fading model.

3.4.1 Increased Signal-to-Noise Ratio

Increased signal-to-noise ratio would reduce the pointing errors that result from the algorithms. Gains are expected at look angles where boundary layer effects spread power across many pixels in the FPA.

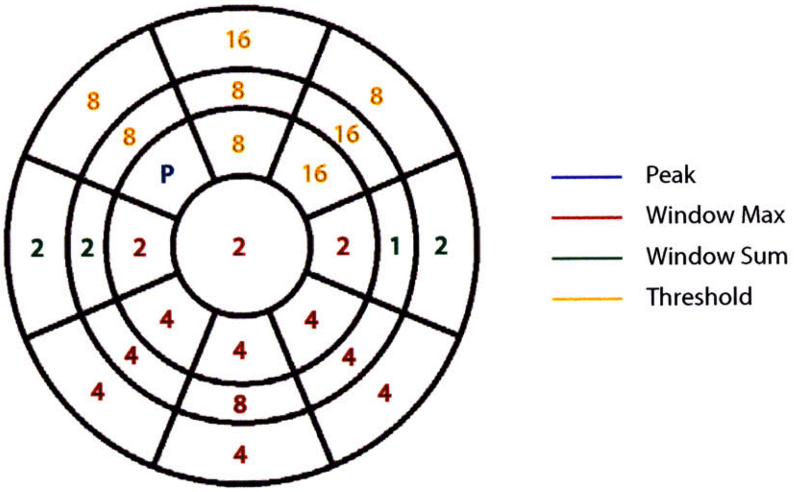

Figure 3-13: Best Algorithm at Each Look Angle at Twice SNR

A plot of the best algorithm at each look angle is shown in Fig. 3-13. The performance plot for each algorithm-parameter pair is shown in Fig. 3-14. Table A.3 contains the tabulated performance values in dB. This table reveals that the maximal gain from doubling the SNR occurs at 90° azimuth and 45° elevation, where the boundary layer often causes power to distribute across multiple peaks on the FPA. The average power sent to the satellite increases by 0.06 dB at this look angle.

The maximal loss while increasing SNR is only 0.01 dB, which suggests that performance gain from the increased SNR is not simply the result of variations in the noise realization. We find that an increase of 3 dB in power to the tracking system yields only marginal gains in pointing.

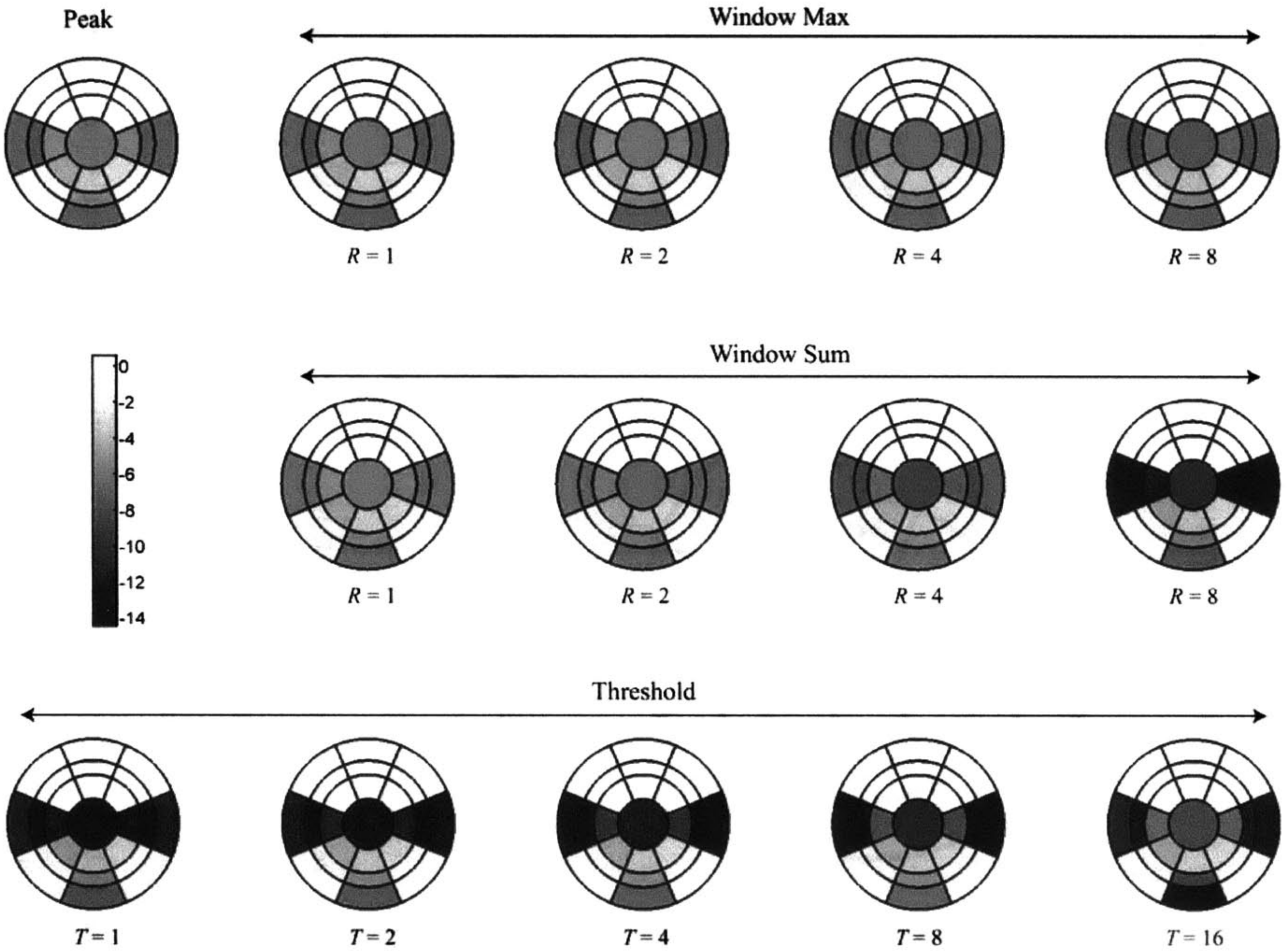

Figure 3-14: Algorithm Performance at Each Look Angle at Twice SNR. Scale in dB.

3.4.2 Decreased Signal-to-Noise Ratio

Pointing errors are expected to increase when the fraction of power sent to the tracking system is reduced by 3 dB. A plot of the best algorithm as a function of look angle is shown in Fig. 3-15 and individual algorithm results are available in Fig. 3-16.

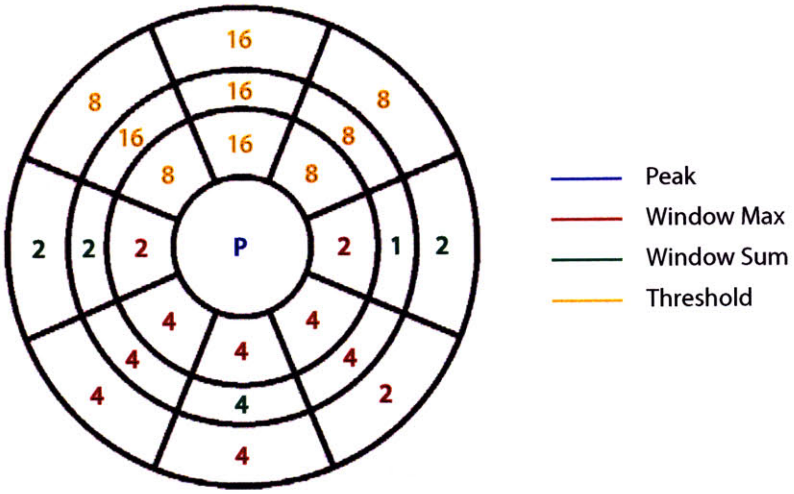

Figure 3-15: Best Algorithm at Each Look Angle at Half SNR

In this case, we again find that there are only marginal changes in performance. The tabulated results are available in Table A.4. The maximum loss over all look angles is 0.08 dB and occurs at -90° azimuth and 15° elevation. We find that the maximum increase in performance is limited to 0.01 dB. Reducing the power to the tracking system by 3 dB yields only a small reduction in performance due to pointing error. This small reduction explains why the performance did not change considerably under stronger atmospheric fading.

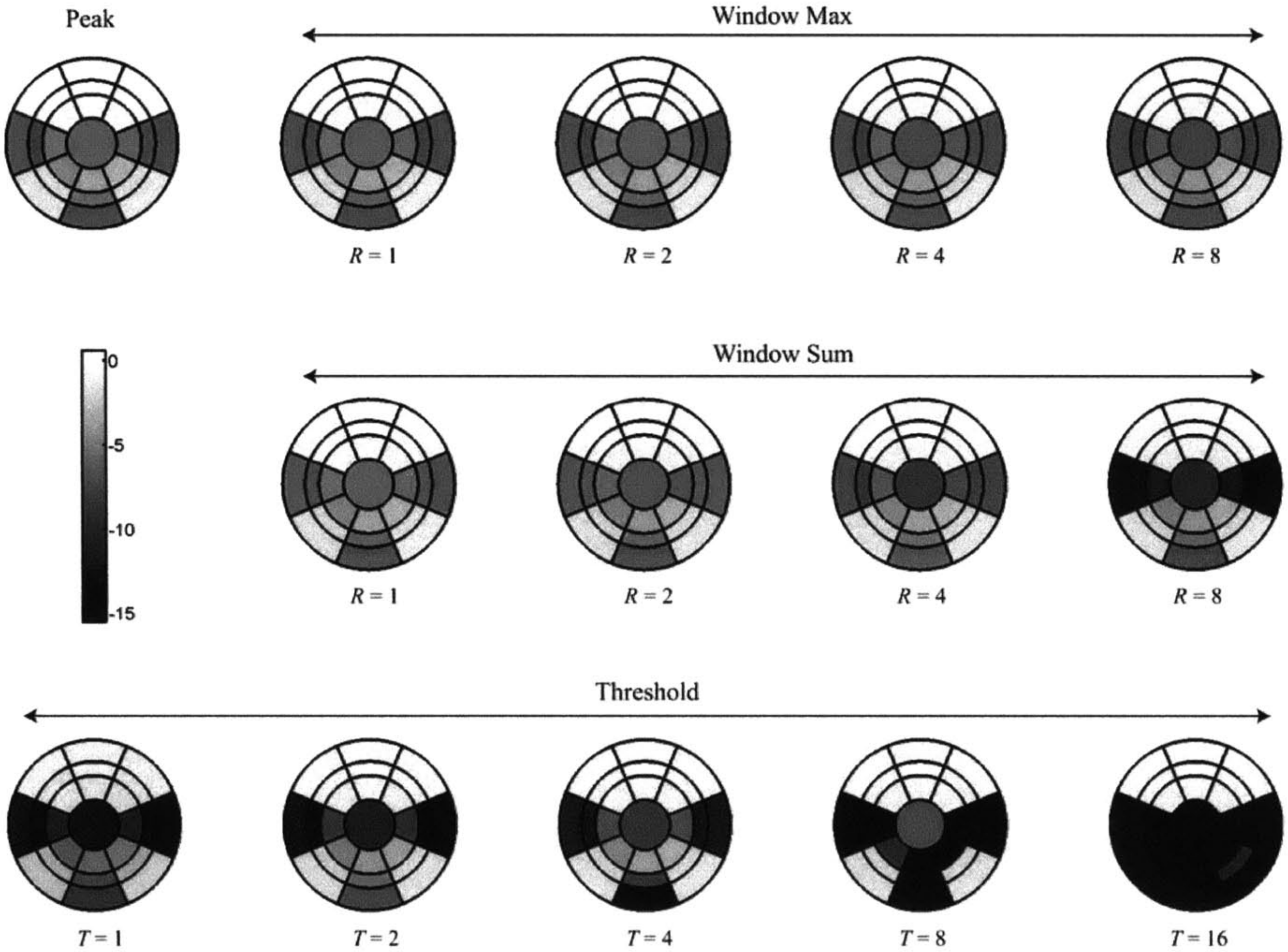

Figure 3-16: Algorithm Performance at Each Look Angle at Half SNR. Scale in dB.

Chapter 4

Conclusion

In this thesis, we have examined the performance of different tracking algorithms in various situations. The results show that the reduction in power to satellite is caused primarily by spreading of the beam due to the boundary layer. Read-out noise and bandwidth constraints imposed by the fast-steering mirror and tracking servo also contribute to degradation in performance. Pointing errors arising from these two components are only negligible in the forward look angles. Variations in the signal-to-noise ratio caused little change in performance, suggesting that bandwidth constraint is the dominant component of pointing error at look angles with significant boundary layer distortions. Atmospheric fading also did not have a significant impact on pointing error.

Using these results, we can consider a robust algorithm choice for a more general set of conditions. We will discuss performance of the different algorithms under different types of boundary layer distortions.

4.1 Forward

In the forward look angles, the beam's ideal Airy distribution is only slightly spread by the boundary layer; tip and tilt constitute most of the phase distortion. Performance in this direction is insensitive to the choice of algorithm. While Threshold performs best in this direction, the improvement over other algorithms would be imperceptible in a real world implementation.

4.2 Side and Top

At look angles to the side and top of the turret, the shock wave distorts the beam such that multiple peaks are imaged on the FPA. Peaks rise and fall as the phase distortions change with time.

Threshold performs especially poor across all threshold levels. In this situation, Threshold is not able to properly estimate a peak for the aircraft to point at; after thresholding, the algorithm will often take the centroid of a distribution with multiple peaks or, should the boundary layer cause the signal to fall below the threshold level, have no distribution at all. This problem arises in part from having a fixed threshold level. A threshold algorithm where the threshold level is set at a fraction of the maximum intensity pixel may be worth investigation.

At these look angles, the peaks are often spaced closely together; thus, a small window size is needed in the windowed centroid algorithms to properly point at a peak. We find that the best algorithms at this look angle are window centroids. The Peak algorithm could be considered a windowed centroid with the smallest window size possible.

It is worth noting that the Window Sum algorithm degrades in performance faster with increasing window size than Window Max. In multi-modal distributions, Window Sum attempts to capture multiple peaks within the window while Window Max remains centered about the maximum intensity pixel. Generally, care must be used in selecting the window size with a multi-modal distribution.

4.3 Downstream

The turbulent wake in this direction causes the beam to change dynamically. The distortions can cause multi-modal distributions with widely separated peaks or even complete beam break-up at times.

In the downstream look angles, algorithms perform quite similarly with the exception of the Threshold algorithm at particular threshold levels. The Threshold algorithm can be close to that of the best algorithm if used with the proper threshold level.

4.4 All Directions

We find that the most sensitive look angles are to the side and top of the turret. This direction would be the limiting case in choosing a robust algorithm for all look angles. A windowed centroid algorithm such as Window Sum with a radius of 1 pixel or Peak perform well across all look angles.

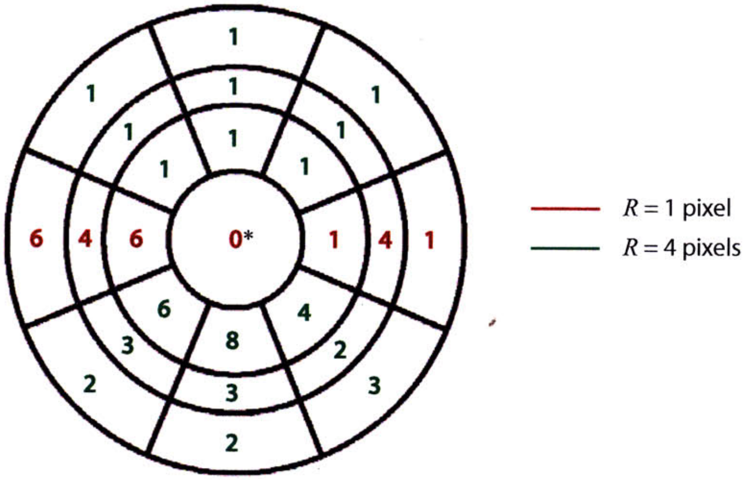

* Best-performing algorithm at the look angle

Figure 4-1: Additional Loss of Window Sum Algorithm with Two Window Sizes. Loss is in Units of 10^{-2} dB.

In the case where we limit ourselves to two algorithms, it would be preferable to have an algorithm with a small window size for look angles to the side and a larger window size for the forward and downstream directions. Fig. 4-1 plots the additional loss over the best-performing algorithm when constrained to the Window Sum algorithm with window sizes of 1 and 4 pixels under moderate atmospheric turbulence. The loss is indicated at each look angle in units of 10^{-2} dB. The color indicates the window size of the Window Sum algorithm. As shown in the plot, we can achieve very small additional losses when constrained to two algorithms for all look angles.

We need to remember that these results are based on a short duration time-series from CFD simulations. Our results may exclude the impact of flow phenomena that occur rarely and were not captured by the CFD results. It would be interesting to examine whether longer time-series simulations match our results. Additionally, simulations with greater reductions in SNR may yield a useful relationship about the power required by the tracking system and pointing error arising from read-out noise.

Appendix A

Tables of Algorithm Performance

Look Angle		**Relative Loss in dB**													
		Peak	Window Max				Window Sum				Threshold				
El	Az	N/A	1	2	4	8	1	2	4	8	1	2	4	8	16
15°	0°	0.00	0.05	0.01	0.00	0.01	0.05	0.01	0.01	0.06	0.32	0.05	0.00	**-0.24**	0.00
15°	45°	0.00	0.05	0.01	0.00	0.01	0.05	0.01	0.01	0.05	0.33	0.05	0.00	0.00	**-0.25**
15°	90°	0.18	0.22	0.20	0.30	0.60	0.01	**6.59**	0.75	6.42	5.92	6.27	7.02	4.81	n/a
15°	135°	0.06	**1.03**	0.00	0.00	0.03	0.01	0.03	0.03	0.10	0.53	0.12	0.05	0.07	0.08
15°	180°	0.16	0.12	0.19	**6.86**	0.09	0.19	0.23	0.02	1.05	1.42	0.57	0.06	n/a	n/a
15°	225°	0.05	0.04	0.04	**1.33**	0.03	0.06	0.06	0.02	0.10	0.63	0.12	0.05	0.07	0.08
15°	270°	0.36	0.32	0.35	0.30	0.95	0.06	**6.42**	1.26	7.00	5.43	5.92	6.28	5.01	n/a
15°	315°	0.00	0.05	0.01	0.00	0.01	0.05	0.01	0.01	0.06	0.32	0.06	0.00	**-0.25**	0.00
25°	0°	0.00	0.05	0.01	0.00	0.01	0.05	0.01	0.01	0.04	0.31	0.04	0.00	**-0.61**	0.00
25°	45°	0.00	0.05	0.01	0.00	0.01	0.05	0.01	0.01	0.05	0.34	0.05	0.00	**-0.04**	0.00
25°	90°	0.45	0.50	0.54	0.50	1.09	0.04	**6.56**	1.46	8.06	6.87	7.89	8.01	5.27	17.64
25°	135°	0.08	0.00	0.03	**1.40**	0.02	0.04	0.06	0.02	0.08	0.71	0.14	0.07	0.09	0.12
25°	180°	0.31	0.35	0.38	0.22	**5.28**	0.42	0.52	0.03	0.47	1.25	0.33	0.04	3.12	n/a
25°	225°	0.07	0.01	0.04	**1.67**	0.03	0.06	0.07	0.03	0.10	0.60	0.13	0.04	0.06	0.09
25°	270°	0.57	0.72	0.79	0.75	1.31	0.04	**6.62**	1.65	6.40	6.18	6.46	6.88	5.39	16.27
25°	315°	0.00	0.05	0.01	0.00	0.01	0.05	0.01	0.01	0.05	0.37	0.06	0.00	**-0.04**	0.00
45°	0°	0.00	0.05	0.01	0.00	0.01	0.05	0.01	0.01	0.06	0.39	0.05	0.00	**-0.02**	0.00
45°	45°	0.00	0.05	0.01	0.00	0.01	0.05	0.01	0.01	0.07	0.45	0.06	0.00	0.00	**0.19**
45°	90°	**5.69**	0.01	0.01	0.61	0.89	0.01	0.91	1.53	6.80	6.07	4.49	2.43	1.32	8.75
45°	135°	0.13	0.06	0.09	**2.91**	0.05	0.07	0.18	0.04	0.17	1.04	0.19	0.04	0.08	n/a
45°	180°	0.10	0.05	0.08	**3.44**	0.13	0.13	0.23	0.08	0.33	1.11	0.28	0.12	0.11	n/a
45°	225°	0.09	0.06	0.10	**4.43**	0.06	0.15	0.30	0.06	0.40	1.19	0.28	0.06	0.09	n/a
45°	270°	0.06	0.09	**5.23**	0.42	1.25	0.06	0.64	1.46	6.40	6.21	4.78	2.70	1.56	9.78
45°	315°	0.00	0.05	0.01	0.00	0.01	0.05	0.01	0.01	0.06	0.36	0.06	0.00	**0.18**	0.00
90°	0°	0.06	0.10	0.03	0.69	1.24	**5.93**	0.57	2.69	4.23	6.46	5.98	4.82	2.48	1.01

Table A.1: Performance Comparison of All Algorithms With Moderate Atmospheric Turbulence. The average power degradation in dB for the best-performing algorithm at each look angle is highlighted. The remaining entries contain the additional degradation experienced by the other algorithms.

Look Angle		Relative Loss in dB													
		Peak	Window Max				Window Sum				Threshold				
El	Az	N/A	1	2	4	8	1	2	4	8	1	2	4	8	16
15°	0°	0.00	0.05	0.01	0.00	0.01	0.05	0.01	0.01	0.05	0.33	0.05	0.00	0.00	**-0.34**
15°	45°	0.00	0.05	0.01	0.00	0.01	0.05	0.01	0.01	0.05	0.28	0.04	0.00	0.00	**-0.76**
15°	90°	0.24	0.21	0.26	0.33	0.71	0.03	**6.27**	0.82	6.13	6.16	6.58	7.25	10.60	n/a
15°	135°	0.06	0.01	0.01	**0.51**	0.03	0.01	0.03	0.02	0.10	0.49	0.12	0.05	0.06	0.07
15°	180°	0.12	0.12	0.15	**6.79**	0.16	0.20	0.24	0.04	1.05	1.40	0.63	0.12	n/a	n/a
15°	225°	0.06	0.05	0.04	**0.74**	0.02	0.06	0.07	0.02	0.07	0.55	0.10	0.05	0.07	3.32
15°	270°	0.39	0.37	0.33	0.39	1.02	0.05	**6.25**	1.22	7.08	4.87	5.28	5.56	10.74	n/a
15°	315°	0.00	0.04	0.01	0.00	0.01	0.05	0.01	0.01	0.05	0.32	0.05	0.00	**-0.76**	0.00
25°	0°	0.00	0.05	0.01	0.00	0.01	0.05	0.01	0.01	0.04	0.29	0.04	0.00	**-0.90**	0.00
25°	45°	0.00	0.05	0.01	0.00	0.01	0.05	0.01	0.01	0.06	0.36	0.06	0.00	**-0.14**	0.00
25°	90°	0.50	0.64	0.49	0.55	1.11	0.08	**6.45**	1.40	7.74	6.94	7.75	7.71	5.12	n/a
25°	135°	0.08	0.00	0.04	**1.32**	0.02	0.03	0.06	0.02	0.07	0.64	0.13	0.06	0.09	0.12
25°	180°	0.30	0.36	0.39	0.20	**5.02**	0.42	0.49	0.03	0.43	1.02	0.30	0.03	n/a	n/a
25°	225°	0.07	0.05	0.04	**1.56**	0.03	0.04	0.06	0.02	0.09	0.60	0.10	0.04	0.06	0.09
25°	270°	0.66	0.72	0.75	0.67	1.23	0.14	**6.52**	1.57	6.32	6.07	6.42	6.75	5.24	n/a
25°	315°	0.00	0.05	0.01	0.00	0.02	0.05	0.01	0.01	0.06	0.37	0.05	0.00	**-0.14**	0.00
45°	0°	0.00	0.05	0.01	0.00	0.01	0.05	0.01	0.01	0.05	0.35	0.05	0.00	**-0.11**	0.00
45°	45°	0.00	0.04	0.01	0.00	0.02	0.05	0.01	0.01	0.06	0.45	0.05	0.00	0.00	**0.17**
45°	90°	0.05	0.04	**5.64**	0.63	0.92	0.05	0.93	1.63	6.73	5.98	4.54	2.52	1.45	n/a
45°	135°	0.11	0.04	0.09	**2.95**	0.04	0.07	0.15	0.04	0.17	0.95	0.17	0.03	0.06	n/a
45°	180°	0.10	0.07	0.10	**3.30**	0.15	0.12	0.23	0.10	0.34	1.02	0.32	0.13	0.13	n/a
45°	225°	0.09	0.04	0.11	**4.56**	0.04	0.15	0.29	0.06	0.41	1.25	0.29	0.06	0.08	n/a
45°	270°	0.03	0.06	**5.26**	0.41	1.17	0.02	0.66	1.34	6.41	5.82	4.73	2.71	1.51	9.24
45°	315°	0.00	0.05	0.01	0.00	0.02	0.05	0.01	0.01	0.06	0.39	0.06	0.00	0.00	**0.16**

Table A.2: Performance Comparison of All Algorithms With Strong Atmospheric Turbulence. The average power degradation in dB for the best-performing algorithm at each look angle is highlighted. The remaining entries contain the additional degradation experienced by the other algorithms.

Look Angle		Relative Loss in dB													
		Peak	Window Max				Window Sum				Threshold				
El	Az	N/A	1	2	4	8	1	2	4	8	1	2	4	8	16
15°	0°	0.00	0.05	0.01	0.00	0.00	0.05	0.01	0.00	0.01	0.09	0.01	0.00	0.00	**-0.24**
15°	45°	0.00	0.05	0.01	0.00	0.00	0.05	0.01	0.00	0.02	0.10	0.01	0.00	**-0.25**	0.00
15°	90°	0.22	0.27	0.22	0.20	0.68	0.04	**6.56**	0.69	6.13	5.25	5.61	6.38	6.96	5.61
15°	135°	0.06	0.00	0.00	**1.03**	0.02	0.02	0.02	0.02	0.06	0.20	0.05	0.04	0.05	0.07
15°	180°	0.14	0.16	0.18	**6.82**	0.12	0.21	0.24	0.07	1.02	1.20	0.77	0.44	0.09	n/a
15°	225°	0.05	0.04	0.04	**1.32**	0.02	0.05	0.07	0.02	0.06	0.24	0.06	0.05	0.06	0.07
15°	270°	0.32	0.28	0.32	0.31	0.89	0.07	**6.42**	1.29	6.84	5.17	5.35	5.94	6.18	4.97
15°	315°	0.00	0.05	0.01	0.00	0.00	0.05	0.01	0.01	0.02	0.10	0.01	0.00	**-0.25**	0.00
25°	0°	0.00	0.05	0.01	0.00	0.00	0.05	0.01	0.00	0.01	0.09	0.01	0.00	**-0.61**	0.00
25°	45°	0.00	0.05	0.01	0.00	0.00	0.05	0.01	0.00	0.02	0.10	0.01	0.00	0.00	**-0.04**
25°	90°	0.42	0.50	0.37	0.54	1.00	**6.55**	0.01	1.61	7.87	6.60	7.21	7.94	7.90	5.14
25°	135°	0.08	0.02	0.03	**1.40**	0.00	0.03	0.07	0.02	0.03	0.23	0.05	0.04	0.07	0.10
25°	180°	0.29	0.35	0.39	0.18	**5.29**	0.41	0.47	0.04	0.44	0.74	0.37	0.18	0.03	3.12
25°	225°	0.07	0.02	0.04	**1.67**	0.02	0.04	0.05	0.03	0.07	0.24	0.05	0.03	0.04	0.06
25°	270°	0.60	0.66	0.63	0.57	1.31	0.08	**6.59**	1.69	6.43	6.01	6.14	6.48	6.92	5.37
25°	315°	0.00	0.05	0.01	0.00	0.00	0.05	0.01	0.00	0.02	0.10	0.01	0.00	**-0.04**	0.00
45°	0°	0.00	0.05	0.01	0.00	0.00	0.05	0.01	0.00	0.01	0.12	0.01	0.00	**-0.02**	0.00
45°	45°	0.00	0.05	0.01	0.00	0.00	0.05	0.01	0.01	0.02	0.14	0.01	0.00	0.00	**0.19**
45°	90°	0.06	0.10	**5.63**	0.64	0.97	0.10	0.94	1.61	7.00	6.63	5.83	4.22	2.40	1.36
45°	135°	0.08	0.04	0.08	**2.92**	0.02	0.06	0.15	0.03	0.15	0.46	0.10	0.03	0.03	0.06
45°	180°	0.11	0.04	0.09	**3.42**	0.17	0.13	0.22	0.11	0.33	0.62	0.25	0.18	0.14	0.14
45°	225°	0.07	0.06	0.08	**4.44**	0.03	0.15	0.27	0.05	0.34	0.72	0.27	0.12	0.06	0.09
45°	270°	0.04	0.06	**5.23**	0.39	1.25	0.05	0.65	1.36	6.68	6.50	5.91	4.40	2.62	1.52
45°	315°	**0.18**	0.05	0.01	0.00	0.00	0.05	0.01	0.01	0.02	0.11	0.01	0.00	0.00	0.00
90°	0°	0.10	0.04	**5.93**	0.69	1.24	0.06	0.65	2.47	4.36	6.60	6.35	5.83	4.80	2.38

Table A.3: Performance Comparison of All Algorithms with Increased SNR. The average power degradation in dB for the best-performing algorithm at each look angle is highlighted. The remaining entries contain the additional degradation experienced by the other algorithms.

Look Angle		Relative Loss in dB														
		Peak	Window Max				Window Sum				Threshold					
El	Az	N/A	1	2	4	8	1	2	4	8	1	2	4	8	16
15°	0°	0.00	0.05	0.01	0.00	0.05	0.05	0.01	0.02	0.19	1.03	0.17	0.00	0.00	**-0.24**
15°	45°	0.00	0.05	0.01	0.00	0.06	0.05	0.01	0.02	0.22	1.11	0.21	0.00	**-0.24**	0.00
15°	90°	0.39	0.31	0.30	0.48	0.96	0.14	**6.65**	0.96	6.53	6.73	6.85	5.18	n/a	n/a
15°	135°	0.05	0.01	**1.03**	0.01	0.08	0.01	0.03	0.04	0.23	1.25	0.30	0.06	0.07	17.97
15°	180°	0.16	0.19	0.21	**6.85**	0.15	0.20	0.23	0.03	1.01	2.37	0.66	n/a	n/a	n/a
15°	225°	0.05	0.04	0.03	**1.33**	0.06	0.04	0.07	0.03	0.20	1.49	0.36	0.06	0.08	14.86
15°	270°	0.36	0.38	0.32	0.32	1.12	0.04	**6.50**	1.15	7.17	6.29	6.24	5.34	n/a	n/a
15°	315°	0.00	0.05	0.01	0.00	0.06	0.05	0.01	0.02	0.22	1.01	0.21	0.00	**-0.25**	0.00
25°	0°	0.00	0.05	0.01	0.00	0.04	0.05	0.01	0.01	0.17	1.02	0.18	0.00	0.00	**0.61**
25°	45°	0.00	0.05	0.01	0.00	0.06	0.05	0.01	0.01	0.21	1.10	0.22	0.00	**-0.04**	0.00
25°	90°	0.53	0.70	0.53	0.55	1.36	**6.60**	0.00	1.30	8.23	6.49	7.81	5.64	18.13	n/a
25°	135°	0.08	0.01	0.04	**1.40**	0.05	0.03	0.07	0.03	0.22	1.80	0.38	0.08	0.11	8.89
25°	180°	0.27	0.36	0.36	0.17	0.04	0.43	0.48	**5.33**	0.52	2.13	0.37	3.05	n/a	n/a
25°	225°	0.07	0.01	0.03	**1.68**	0.07	0.03	0.05	0.04	0.24	1.62	0.30	0.05	0.08	n/a
25°	270°	0.80	0.76	0.76	0.84	1.62	0.09	**6.67**	1.73	6.55	6.66	6.72	5.50	12.67	n/a
25°	315°	0.00	0.05	0.01	0.00	0.06	0.05	0.01	0.02	0.24	1.14	0.23	0.00	0.00	**-0.04**
45°	0°	0.00	0.05	0.01	0.00	0.06	0.05	0.01	0.02	0.23	1.20	0.22	0.00	0.00	**-0.02**
45°	45°	0.00	0.05	0.01	0.00	0.06	0.05	0.01	0.02	0.23	1.19	0.24	0.00	**0.19**	0.00
45°	90°	0.00	0.05	**5.72**	0.61	0.88	0.02	0.79	1.65	6.29	5.27	3.28	1.34	n/a	n/a
45°	135°	0.1	0.05	0.06	**2.92**	0.11	0.03	0.15	0.04	0.33	2.41	0.44	0.05	n/a	n/a
45°	180°	0.09	0.04	0.06	**3.46**	0.16	0.09	0.20	0.09	0.43	2.26	0.55	0.09	n/a	n/a
45°	225°	0.09	0.08	0.15	**4.42**	0.08	0.14	0.31	0.08	0.57	2.25	0.56	0.08	5.24	n/a
45°	270°	0.06	0.09	**5.28**	0.42	1.29	0.08	0.60	1.39	6.32	5.60	3.41	1.66	9.72	n/a
45°	315°	0.00	0.05	0.01	0.00	0.06	0.05	0.01	0.02	0.23	1.13	0.23	0.00	**0.18**	0.00
90°	0°	**5.98**	0.03	0.00	0.80	1.31	0.05	0.54	2.93	4.14	6.73	5.29	2.72	0.98	n/a

Table A.4: Performance Comparison of All Algorithms with Reduced SNR. The average power degradation in dB for the best-performing algorithm at each look angle is highlighted. The remaining entries contain the additional degradation experienced by the other algorithms.

Bibliography

[1] U. Frisch. *Turbulence: The Legacy of A.N. Kolmogorov.* Cambridge University Press, Cambridge, 1995.

[2] J. W. Goodman. *Introduction to Fourier Optics.* Roberts & Co., Englewood, CO, 3rd edition, 2005.

[3] S. Gordeyev, T. E. Hayden, and E. J. Jumper. Aero-optical and flow measurements over a flat-windowed turret. *AIAA Journal*, 45(2):347–357, Feb 2007.

[4] Y. Hsia, W. Lin, H. Loh, P. Lin, D. Nahrstedt, and J. Logan. CFD-based aero-optical performance prediction of a turret. In *Proceedings of SPIE - The International Society for Optical Engineering*, pages 143–154, Orlando, FL, United States, 2005.

[5] S. Michael. Simulated time series of lasercom uplink receiver power: Airplane to geosynchronous satellite. Technical report, MIT Lincoln Laboratory, July 2005.

[6] M. C. Roggemann. *Imaging Through Turbulence.* The CRC Press laser and optical science and technology series. CRC Press, Boca Raton, 1996.

[7] V. I. Tatarskii. *Wave Propagation in a Turbulent Medium.* McGraw-Hill, New York, 1961.

3570 · 90